mathematics

MDPI

Article

Numerical Modeling of a Gas–Particle Flow Induced by the Interaction of a Shock Wave with a Cloud of Particles

Konstantin Volkov

Department of Mechanical Engineering, Kingston University, London SW15 3DW, UK; k.volkov@kingston.ac.uk

Abstract

A continuum model for describing pseudo-turbulent flows of a dispersed phase is developed using a statistical approach based on the kinetic equation for the probability density of particle velocity and temperature. The introduction of the probability density function enables a statistical description of the particle ensemble through equations for the first and second moments, replacing the dynamic description of individual particles derived from Langevin-type equations of motion and heat transfer. The lack of detailed dynamic information on individual particle behavior is compensated by a richer statistical characterization of the motion and heat transfer within the particle continuum. A numerical simulation of the unsteady flow of a gas–particle suspension generated by the interaction of a shock wave with a particle cloud is performed using an interpenetrating continua model and equations for the first and second moments of both gas and particles. Numerical methods for solving the two-phase gas dynamics equations—formulated using a two-velocity and two-temperature model—are discussed. Each phase is governed by conservation equations for mass, momentum, and energy, written in a conservative hyperbolic form. These equations are solved using a high-order Godunov-type numerical method, with time discretization performed by a third-order Runge–Kutta scheme. The study analyzes the influence of two-dimensional effects on the formation of shock-wave flow structures and explores the spatial and temporal evolution of particle concentration and other flow parameters. The results enable an estimation of shock wave attenuation by a granular backfill. The extended pressure relaxation region is observed behind the cloud of particles.

Keywords: gas–particle flow; numerical simulation; shock wave; particle; fraction; cloud of particles; interaction

MSC: 35Q; 65M

check for updates

Academic Editor: Cesáreo González

Received: 30 September 2025
Revised: 21 October 2025
Accepted: 25 October 2025
Published: 28 October 2025

Citation: Volkov, K. Numerical Modeling of a Gas–Particle Flow Induced by the Interaction of a Shock Wave with a Cloud of Particles. *Mathematics* **2025**, *13*, 3427. https://doi.org/10.3390/math13213427

Copyright: © 2025 by the author. Licensee MDPI, Basel, Switzerland. This article is an open access article distributed under the terms and conditions of the Creative Commons Attribution (CC BY) license (https://creativecommons.org/licenses/by/4.0/).

1. Introduction

Problems such as the formation of particle clouds, dust lifting behind passing shock waves, and particle ignition in high-speed, high-temperature flows are of great practical importance [1–3]. The characteristic features of shock-wave phenomena (large dynamic loads, high flow velocities, complex wave structures, abrupt temporal and spatial variations in flow parameters, and a wide range of characteristic scales) make experimental investigation particularly challenging. The required facilities and equipment are complex and costly to design and operate. Moreover, the data obtained from such experiments are often incomplete and must be complemented by theoretical analysis and numerical modeling. Advances in computational technologies now make it possible to simulate and

visualize detailed two- and three-dimensional flow structures, revealing both local features and global characteristics of these processes [4].

Pseudo-turbulent flow (also called pseudo-turbulence or particle-induced turbulence) refers to velocity fluctuations and apparent turbulent-like motion that arise not from fluid instability, but from the disturbances generated by the motion of solid particles within an otherwise laminar or weakly turbulent flow.

When a shock wave propagates along a particle layer, vortex structures are generated—similar to those that appear during the interaction of oblique shock waves with thermal or liquid layers [5]. The instability of the layer surface develops, resulting in the formation of vortical structures that lift material from the layer and promote gas mixing. Mathematical aspects of modeling such two-phase flows, including the formulation of the Cauchy problem for the governing equations, are discussed in [6–8].

A two-dimensional flow behind a passing shock wave in a region containing irregularly distributed stationary cylinders was numerically simulated in [9,10]. This configuration qualitatively corresponds to the dense dust sheet investigated experimentally in [11]. The dispersed-phase volume fraction was 15%, which precludes the use of a point-particle model typically applied to dilute particle clouds where particle–particle interactions are negligible [12]. Cross-sectional averaging of the obtained results allowed comparison with a one-dimensional model, revealing that while the latter adequately reproduces the overall steady-flow behavior, it fails to capture the significant unsteady effects within and behind the particle cloud.

When the incident shock wave reaches the leading edge of the particle cloud and begins to penetrate it, a reflected wave forms and propagates opposite to the incident shock, while a transmitted shock wave continues in the same direction. Within the cloud, a fan of rarefaction waves develops behind the transmitted shock. As the transmitted wave exits the cloud, a second rarefaction fan forms inside it, and a contact discontinuity emerges from the cloud along with the transmitted wave, separating it from the rarefaction region [9,10]. Over time, a steady pressure gradient is established within the cloud.

Two-dimensional simulations based on a Lagrangian description of the dispersed phase were performed in [13,14], examining the interaction of a shock wave with particle clouds of various initial shapes. The initial particle concentration in the cloud was assumed to be 0.04%. A continuum description of both the gas and dispersed phases was employed in [15,16] for two-dimensional simulations and in [17,18] for three-dimensional modeling. In [19], three-dimensional calculations were conducted for different Mach numbers of the incident shock wave (ranging from 2.2 to 3), particle volume concentrations (0.05–0.1), and particle diameters (50–100 μm). The results indicate that Reynolds stresses play a key role in the momentum balance at the cloud boundary and significantly influence the intensity of the reflected shock wave. The magnitude of the Reynolds stresses depends strongly on particle concentration and only weakly on particle size.

In the experimental study [20], the characteristics of the transmitted and reflected shock waves generated by the passage of an incident shock wave through a layer of solid particles in a shock tube were investigated. The Mach number of the incident wave, the backfill thickness (L), the backfill permeability (S), and the particle diameter (D) were varied. The measurement results were analyzed as dependencies of the intensities of the transmitted and reflected shock waves on the dimensionless parameter $\theta = 1.75(1 - S)L/(SD)$ which characterizes the permeability of the particle layer, for different Mach numbers of the incident shock wave.

In one-dimensional simulations, a region of constant pressure is absent in the reflected wave, owing to the influence of disturbances reflected from downstream obstacles [21]. The calculations show a sharp pressure drop at the right boundary of the particle cloud,

which is clearly observed in two-dimensional simulations but is much less pronounced in the one-dimensional case. This two-dimensional effect is attributed to the contribution of Reynolds stresses within the particle cloud and in its turbulent wake. To account for this phenomenon, [10] introduced an additional term into the right-hand side of the one-dimensional system of equations. The study [22] demonstrated that, for the same incident shock-wave intensity (Mach number 1.5), a system of spheres attenuates the shock wave more effectively than an array of equally spaced cylinders of comparable diameter.

When modeling particle motion in a rarefied dispersed medium—characterized by a low volume concentration of the dispersed phase—attention is primarily focused on the interaction between particles and the turbulent vortices of the carrier flow, since particle–particle interactions are negligible. As the concentration and size of the particles increase, however, interparticle interactions begin to make a significant contribution to the transfer of momentum and energy within the dispersed phase. The chaotic particle motion arising from these interactions is referred to as pseudo-turbulence, to distinguish it from turbulence induced by the carrier flow itself.

Pseudo-turbulent fluctuations originate from two main mechanisms: hydrodynamic interactions between particles (mediated by random exchanges of momentum and energy with the fluctuating velocity and pressure fields of the surrounding medium) and direct particle collisions. With increasing particle concentration and size, the contribution of collisional momentum and energy exchange becomes dominant over hydrodynamic interactions. In highly concentrated dispersed media, interparticle collisions play a decisive role in shaping the statistical properties of the system [23].

The processes of particle interaction with turbulent vortices and interparticle collisions can be treated as statistically independent only for inertial particles, whose dynamic relaxation time is much longer than the characteristic time of interaction with turbulent vortices. In this case, the relative motion of particles is uncorrelated and resembles the chaotic motion of molecules. For low-inertia particles, however, the mutual influence of particle–turbulence and particle–particle interactions must be taken into account.

Fluctuations in the dispersed phase are defined as deviations from the mean velocity and should not be confused with turbulent fluctuations. The temporal and spatial characteristics of pseudo-turbulence in the dispersed phase differ significantly from those of conventional turbulence [24,25].

The statistical approach based on the kinetic equation for the probability densities of particle velocity, temperature, and other relevant characteristics provides the most consistent framework for constructing continuum models of pseudo-turbulent flows in dispersed media, where fluctuations arise from the random configuration of particles. The introduction of a probability density function (PDF) enables a statistical description of the particle ensemble, replacing the dynamic description of individual particles based on Langevin-type equations of motion and heat transfer.

The model proposed in [26–29] and further developed in [30,31] for the numerical simulation of unsteady gas flows with inert particles is employed in this study. The introduction of the probability density function enables a statistical description of the particle system, replacing the dynamic description of individual particles based on Langevin-type stochastic equations. The continuity, momentum, and energy equations for both the gas and dispersed phases are hyperbolic and are solved using a high-order Godunov-type numerical method. The flow structure and the spatiotemporal evolution of flow parameters during the interaction of a supersonic flow with a particle layer are computed, and the results are compared with data obtained from a one-dimensional formulation of the problem.

2. Mathematical Model

The equations governing the motion and heat transfer of the dispersed phase are derived from the Liouville equation for the probability density function of particle distributions in position, velocity, and temperature. To close the resulting system of equations, third-order correlation moments of particle velocity and temperature are neglected. In the formulation of the governing equations, the indices g and p denote the gas and particle phases, respectively.

2.1. Discrete Model

The equations governing the motion and heat transfer of a test particle are stochastic Langevin-type equations that depend on the random velocity $\mathbf{v}_g$ and temperature T_g fields of the carrier flow. The carrier-gas velocity and temperature are evaluated at points along the particle trajectory. The equations describing the motion and heat transfer of an individual particle take the following form [2]

$$\frac{d\boldsymbol{x}_p}{dt} = \boldsymbol{v}_p; \tag{1}$$

$$m_p \frac{d\boldsymbol{v}_p}{dt} = \boldsymbol{f}_p; \tag{2}$$

$$c_p^m m_p \frac{dT_p}{dt} = q_p. \tag{3}$$

Here, t is time, $\boldsymbol{x}_p$ is radius vector of the particle center of mass, $\boldsymbol{v}_p$ is particle velocity, T_p is particle temperature, $\boldsymbol{f}_p$ is force acting on the particle, q_p is convective heat flow between the gas and the particle, m_p is particle mass, c_p^m is specific heat capacity of the particle material.

The drag force is expressed as

$$\boldsymbol{f}_p = \frac{1}{2} C_D \rho_g |\boldsymbol{v}_g - \boldsymbol{v}_p| (\boldsymbol{v}_g - \boldsymbol{v}_p) S_m,$$

where ρ is density, S_m is area of of the midsection of the particle. The drag coefficient is represented as

$$C_D = C_{D0} f_D,$$

where $C_{D0} = 24/\mathrm{Re}_p$ is the drag coefficient corresponding to Stokes law, f_D is a function taking into account the correction for the particle inertia and compressibility. The correction function is represented as [2]

$$f_D = \left(1 + 0.15\mathrm{Re}_p^{0.687}\right)\left[1 + \exp\left(-\frac{0.427}{\mathrm{M}_p^{4.63}} - \frac{3}{\mathrm{Re}_p^{0.88}}\right)\right].$$

Reynolds and Mach numbers are calculated from the relative velocity of gas and particles

$$\mathrm{Re}_p = \frac{2\rho_g r_p |\boldsymbol{v}_g - \boldsymbol{v}_p|}{\mu}, \quad \mathrm{M}_p = \frac{|\boldsymbol{v}_g - \boldsymbol{v}_p|}{c},$$

where r_p is particle radius, μ is dynamic viscosity, c is local speed of sound. For a spherical particle of radius r_p, $S_m = \pi r_p^2$ and $m_p = 4\pi r_p^3 \rho_p / 3$. Equation (2) is represented as

$$\frac{d\boldsymbol{v}_p}{dt} = \frac{f_D}{\tau_v}(\boldsymbol{v}_g - \boldsymbol{v}_p). \tag{4}$$

Here, $\tau_v = \rho_p d_p^2/(18\mu)$ is the dynamic relaxation time.

Expressing the heat-transfer coefficient in terms of the Nusselt number, $h = \mathrm{Nu}_p \lambda_p / d_p$, the convective heat flux between the gas and a particle can be written as [2]

$$q_p = \mathrm{Nu}_p \lambda (T_g - T_p) \frac{S_p}{d_p},$$

where S_p is the particle surface area, λ is the thermal conductivity of the gas. The Nusselt number is represented in a form taking into account the correction for the particle inertia

$$\mathrm{Nu}_p = 2 + 0.459 \mathrm{Re}_p^{0.55} \mathrm{Pr}^{0.33},$$

where Pr is Prandtl number (for air Pr = 0.72). Equation (3) is represented as

$$\frac{dT_p}{dt} = \frac{1}{\tau_\vartheta}(T_g - T_p). \tag{5}$$

Here, $\tau_\vartheta = c_p \rho_p d_p / (3\lambda \mathrm{Nu}_p)$ is the thermal relaxation time, $\tau_\vartheta = (3\mathrm{Pr}\beta/\mathrm{Nu}_p)\tau_v$, where $\beta = c_p^m / c_p$ is the ratio of the specific heat of the dispersed phase to the specific heat of the gas at constant pressure.

In dimensionless variables, the dynamic and thermal relaxation times are replaced by Stokes numbers

$$\mathrm{Stk}_v = \frac{2\rho_p r_p^2 U}{9\mu L}, \quad \mathrm{Stk}_\vartheta = \frac{2 c_p \rho_p r_p U}{3\lambda \mathrm{Nu}_p L},$$

where L and U are characteristic scales of length and velocity. The characteristic length and velocity for the study considered are the length of particle cloud and velocity on inlet boundary of computational domain.

2.2. Continuum Model

The statistical approach based on the kinetic equation for the probability density function (PDF) of particle velocities, temperatures, and other relevant characteristics provides the most consistent framework for constructing continuum models of pseudo-turbulent flows in dispersed media. The introduction of a PDF enables a statistical description of a particle ensemble, replacing the dynamic description of individual particles based on Langevin-type equations of motion and heat transfer [30]. While statistical modeling inherently loses some information about the behavior of individual particles, this loss is compensated by a richer characterization of the statistical patterns of motion and heat transfer within the dispersed phase as a whole.

To derive the equations governing the motion and heat transfer of a particle continuum, the approach proposed in [32] for simulating large eddies in turbulent gas–particle flows is employed, along with its generalization developed in [28,29] for direct numerical modeling of two-phase flows. Within this continuum framework, the continuity equation, the momentum equation, and the temperature evolution equation of the dispersed phase are obtained from the Lagrangian equations of motion and heat transfer for an individual particle, as expressed in Equations (1), (4) and (5). It is assumed that $f_D = 1$ and $\mathrm{Nu}_p = 2$ for simplicity.

The use of the Stokes drag model and heat conduction only energy exchange does not, by itself, require neglecting gas–particle velocity slip. In fact, the presence of slip velocity is an inherent part of the drag formulation. The Stokes drag law is valid only for low particle Reynolds numbers, where the slip velocity is small enough that inertial and non-linear drag effects can be neglected. No additional unsteady or compressibility effects (e.g., Basset

history term, pressure gradient forces, or shock-induced drag enhancement) are considered. In the energy equation, only heat conduction between the gas and particles is included, neglecting convective and radiative contributions, which are secondary for small particles and short interaction times. Therefore, while the model includes velocity slip, it assumes that this slip remains within the creeping-flow regime, where Stokes drag and conductive heat transfer provide an adequate description of interphase coupling. This simplification is appropriate for dilute particle clouds with small particles and moderate shock strengths but may require correction for larger particles or stronger shocks.

To transition from the dynamic, stochastic Langevin-type Equations (Lagrangian description) to a statistical description of the particle system in terms of spatial, velocity, and temperature distributions (Eulerian description), a dynamic probability density function is introduced in the phase space of particle coordinates, velocities, and temperatures

$$w_i(\boldsymbol{x}_p, \boldsymbol{v}_p, \vartheta_p, t) = \delta\Big[\boldsymbol{x}_p - \boldsymbol{x}_{pi}(t)\Big]\delta\Big[\boldsymbol{v}_p - \boldsymbol{v}_{pi}(t)\Big]\delta\Big[\vartheta_p - \vartheta_{pi}(t)\Big],$$

where $\boldsymbol{v}_p$, ϑ_p are the velocity and temperature of the dispersed phase, which are the realization of a random field of velocity and temperature at point $\boldsymbol{x}_p$ at time t, $\boldsymbol{v}_{pi}$, ϑ_{pi} are parameters that play the role of independent variables.

At time t, the state of a system of N particles is determined by specifying the values of the coordinates $\boldsymbol{x}_{p1}, \ldots, \boldsymbol{x}_{pN}$, the velocities $\boldsymbol{v}_{p1}, \ldots, \boldsymbol{v}_{pN}$, and the temperatures $\vartheta_{p1}, \ldots, \vartheta_{pN}$ of all particles. The set of coordinates, velocities and temperatures of an individual particle is denoted by $\boldsymbol{z}_{pi} = (\boldsymbol{x}_{pi}, \boldsymbol{v}_{pi}, \vartheta_{pi})$, where $i = 1, \ldots, N$, and the set of coordinates, velocities and temperatures of all particles in the system is denoted by $Z = (\boldsymbol{z}_{p1}, \ldots, \boldsymbol{z}_{pN})$.

Assuming the particles are statistically independent, a single-point dynamic probability density function is defined

$$w(\boldsymbol{x}_p, \boldsymbol{v}_p, \vartheta_p, t) = \frac{V_p}{V_\Sigma}\sum_{i=1}^{N} w_i(\boldsymbol{x}_p, \boldsymbol{v}_p, \vartheta_p, t),$$

where V_p is particle volume, V_Σ is system volume. Local functions of dynamic variables depending on the position of the point $z_p = z_p(\boldsymbol{x}_p, \boldsymbol{v}_p, \vartheta_p)$ in phase space are expressed through the microscopic phase density in the space of coordinates, velocities, and temperatures of particles, which satisfies the normalization condition

$$\int w(\boldsymbol{x}_p, \boldsymbol{v}_p, \vartheta_p, \tau) d\boldsymbol{x}_p d\boldsymbol{v}_p d\vartheta_p = 1.$$

It is assumed that $z_p = (\boldsymbol{x}_p, \boldsymbol{v}_p, \vartheta_p)$ and $z_{pi} = (\boldsymbol{x}_{pi}, \boldsymbol{v}_{pi}, \vartheta_{pi})$. Therefore,

$$w(x, t) = \sum_{i=1}^{N} \delta\Big[z_p - z_{pi}(t)\Big].$$

The evolution of the distribution function of the macroscopic states of the system results from the temporal changes in the positions $z_{p1}, \ldots, z_{pN}$, which characterize the state of the system at different times. By differentiating the dynamic probability density in phase space with respect to time, applying the Lagrangian equations of motion and heat transfer for a test particle, and summing over $i = 1, \ldots, N$, the stochastic Liouville equation can be written as [32,33]

$$\frac{\partial W}{\partial t} + \frac{\partial}{\partial x_i}(v_i W) - \frac{\partial}{\partial v_i}\left(\frac{v_i - u_i}{\tau_v} W\right) - \frac{\partial}{\partial \vartheta}\left(\frac{\vartheta - T}{\tau_\vartheta} W\right) = 0, \tag{6}$$

where x_i, v_i and ϑ are the coordinate, velocity, and temperature of the particle. Summation is assumed over the repeating indices.

The averaging operator (spatial filtering operator) is defined by the relation

$$\overline{f}(\boldsymbol{x}) = \int f(\boldsymbol{\xi}) H_\Delta(\boldsymbol{x} - \boldsymbol{\xi}) d\boldsymbol{\xi},$$

where $\overline{f}$ is the mean value of f, H_Δ is the filter (kernel function). The kernel is non-negative and satisfies the normalization condition. The filter width Δ is chosen small enough and such that for the gas phase the relation $\widetilde{\boldsymbol{v}}_g = \boldsymbol{v}_g$ is satisfied. The gas variables are not affected by subgrid fluctuations; therefore, $\widetilde{u_i W} = u_i \widetilde{W}$ and $\widetilde{TW} = T\widetilde{W}$. With a non-negative kernel (top-hat filter, Gaussian filter), the function $\overline{W}$ satisfies the requirements imposed on the probability density function [34,35].

Let Z denote the set of coordinates, velocities, and temperatures of all particles in the system, and $\mathcal{Z}$ be the set of spatial coordinates, velocities, and temperatures in the phase space. Along with the probability density function of the states of the particle system $\delta[\mathcal{Z} - Z(t)]$, the average probability density function of the states of the system $\overline{W}(\mathcal{Z}, t)$ is introduced. It follows from the definition of the averaging operation that

$$\widetilde{\boldsymbol{v}_{pi} w} = \boldsymbol{v}\overline{W}, \quad \widetilde{\vartheta_{pi} w} = \vartheta \overline{W}.$$

By averaging the Liouville equation over an ensemble of random realizations of the velocity and temperature fields, a statistical description of the particle system is obtained. Applying the averaging operator to Equation (6) yields the filtered Liouville equation:

$$\frac{\partial \overline{W}}{\partial t} + \frac{\partial}{\partial x_i}(v_i \overline{W}) - \frac{\partial}{\partial v_i}\left(\frac{v_i - u_i}{\tau_v}\overline{W}\right) - \frac{\partial}{\partial \vartheta}\left(\frac{\vartheta - T}{\tau_\vartheta}\overline{W}\right) = 0. \tag{7}$$

The stochastic Liouville equation, due to its linearity, has the same form for the functions $W(\mathcal{Z}, t)$ and $\overline{W}(\mathcal{Z}, t)$. The average particle number density $\widetilde{\alpha}$, the average velocity $\widetilde{v}_i$ and the average temperature $\widetilde{\vartheta}$ of the dispersed phase are found from the relations

$$\widetilde{\alpha}(\boldsymbol{x}, t) = \int \overline{W}(\boldsymbol{x}, \boldsymbol{v}, \vartheta, t) d\boldsymbol{v} d\vartheta;$$
$$\widetilde{v}_i(\boldsymbol{x}, t) = \frac{1}{\widetilde{\alpha}} \int v_i \overline{W}(\boldsymbol{x}, \boldsymbol{v}, \vartheta, t) d\boldsymbol{v} d\vartheta;$$
$$\widetilde{\vartheta}(\boldsymbol{x}, t) = \frac{1}{\widetilde{\alpha}} \int \vartheta \overline{W}(\boldsymbol{x}, \boldsymbol{v}, \vartheta, t) d\boldsymbol{v} d\vartheta.$$

Equation (7) provides a basis for deriving the equations for the first- and second-order moments of the dispersed phase. The transport equations for the single-point moments of the fluctuating characteristics of the dispersed phase are obtained by multiplying the kinetic equation by a weight function and integrating over the phase subspace of velocities.

The first-order moments represent the mean values of the gas-dynamic parameters of the flow, which depend on spatial and temporal position. The corresponding equations for the first-order moments take the following form:

$$\frac{\partial \widetilde{\alpha}}{\partial t} + \frac{\partial \widetilde{\alpha} \widetilde{v}_i}{\partial x_i} = 0; \tag{8}$$

$$\frac{\partial \widetilde{\alpha} \widetilde{v}_i}{\partial t} + \frac{\partial \widetilde{\alpha} \widetilde{v_j v_i}}{\partial x_j} = \frac{1}{\tau_v} \widetilde{\alpha}(u_i - \widetilde{v}_i); \tag{9}$$

$$\frac{\partial \widetilde{\alpha} \widetilde{\vartheta}}{\partial t} + \frac{\partial \widetilde{\alpha} \widetilde{\vartheta v_i}}{\partial x_i} = \frac{1}{\tau_\vartheta} \widetilde{\alpha}(T - \widetilde{\vartheta}). \tag{10}$$

Single-point second-order correlation moments characterize the kinetic energy of pseudo-turbulence as well as the transport of momentum and heat within the dispersed phase. Two-point second-order moments describe the turbulence spectrum and the scale of large turbulent eddies, providing information on the correlation of fluctuations of various quantities at spatial and temporal points separated by finite distances. The transport equations for the second-order moments take the following form:

$$\frac{\partial \widetilde{\alpha}\widetilde{v_i v_j}}{\partial t} + \frac{\partial \widetilde{\alpha}\widetilde{v_i v_j v_k}}{\partial x_k} = \frac{1}{\tau_v}\widetilde{\alpha}(u_i\widetilde{v}_j + \widetilde{v}_i u_j - 2\widetilde{v_i v_j}); \tag{11}$$

$$\frac{\partial \widetilde{\alpha}\widetilde{\vartheta v_i}}{\partial t} + \frac{\partial \widetilde{\alpha}\widetilde{\vartheta v_i v_k}}{\partial x_k} = \frac{1}{\tau_v}\widetilde{\alpha}(\widetilde{\vartheta}u_i - \widetilde{\vartheta v_j}) + \frac{1}{\tau_\vartheta}\widetilde{\alpha}(T\widetilde{v}_i - \widetilde{\vartheta v_j}). \tag{12}$$

2.3. Model Closure

The components of the subgrid stress tensor and the subgrid heat flux vector are given by:

$$\sigma_{ij} = \widetilde{v_i v_j} - \widetilde{v}_i\widetilde{v}_j, \quad q_i = \widetilde{\vartheta v_i} - \widetilde{\vartheta}\widetilde{v}_i.$$

The averaging procedure for the parameters of the dispersed phase introduces new terms that require modeling. To close Equations (11) and (12), it is assumed that the contributions of third-order correlation moments are negligibly small [32]

$$\int (v - \widetilde{v}_i)(v - \widetilde{v}_j)(v - \widetilde{v}_k)\overline{W}(\boldsymbol{x}, \boldsymbol{v}, \vartheta, t)d\boldsymbol{v}d\vartheta = 0;$$

$$\int (\vartheta - \widetilde{\vartheta})(v - \widetilde{v}_i)(v - \widetilde{v}_k)\overline{W}(\boldsymbol{x}, \boldsymbol{v}, \vartheta, t)d\boldsymbol{v}d\vartheta = 0.$$

By applying the approaches proposed in [29,32] for evaluating integrals, the equations for the third-order moments are replaced with algebraic relations

$$\widetilde{v_i v_j v_k} = \widetilde{v_j v_k}\widetilde{v}_i + \widetilde{v_i v_j}\widetilde{v}_k + \widetilde{v_i v_k}\widetilde{v}_j - 2\widetilde{v}_i\widetilde{v}_j\widetilde{v}_k; \tag{13}$$

$$\widetilde{\vartheta v_i v_k} = \widetilde{\vartheta v_k}\widetilde{v}_i + \widetilde{\vartheta v_i}\widetilde{v}_k + \widetilde{v_i v_k}\widetilde{\vartheta} - 2\widetilde{v}_i\widetilde{v}_k\widetilde{\vartheta}. \tag{14}$$

Relations (13) and (14) provide a closed formulation of the problem.

The motion and heat transfer of the dispersed phase are described by Equations (8)–(10) for the variables $\widetilde{\alpha}$, $\widetilde{v}_i$ and $\widetilde{\vartheta}$, as well as by Equations (11) and (12) for the second-order moments $\widetilde{v_i v_j}$ and $\widetilde{\vartheta v_i}$.

Neglecting inertial effects ($\tau_v = \tau_\vartheta = 0$), the velocity and temperature of the dispersed phase coincide with the corresponding gas parameters ($\widetilde{v}_i = u_i$, $\widetilde{\vartheta} = T$). In this limit, only the transport equation for the particle number density (8) needs to be solved, while the momentum and energy transport Equations (9)–(12) are no longer required.

Partial consideration of inertial effects can be achieved within the equilibrium model, in which the local velocity of the dispersed phase is expressed as the sum of the local gas velocity and the gas acceleration. The particle's dynamic and thermal relaxation times are used as expansion parameters. By assuming $\widetilde{v_i v_j} = \widetilde{v}_i\widetilde{v}_j$ and using Equations (8) and (9), the local acceleration of the dispersed phase is taken to be equal to the local acceleration of the gas. While the equilibrium model captures certain inertial effects, such as preferential acceleration, it is primarily suitable for describing the motion of relatively small particles.

A full account of inertial effects is achieved by solving the transport Equations (8)–(11), while assuming that the contributions of the correlation moments described in Equations (12) and (13) are negligibly small. In practice, this corresponds to $\widetilde{v_i v_j} = \widetilde{v}_i\widetilde{v}_j$ and $\widetilde{\vartheta v_j} = \widetilde{\vartheta}\widetilde{v}_j$. Under these assumptions, the mathematical model is equivalent to the one

proposed in [36], which describes gas–particle flows with a negligibly small particle volume fraction and a sufficiently large density ratio between the dispersed and gas phases. For a gas–particle flow with monodisperse particles, the model equations coincide with those formulated in [37,38].

Although this approach accounts for inertial effects, neglecting the second-order correlation moments of the dispersed phase prevents the capture of several important phenomena, such as the trajectory-crossing effect, which play a significant role in flows of gas suspensions containing highly inertial particles.

3. Two-Dimensional Model

The equations governing the two-dimensional flow of an inviscid compressible gas containing particles are considered. Viscous forces are accounted for only in the interaction between the gas and particles. In the formulation, the indices g and p refer to the gas and particle phases, respectively.

3.1. Equations of Gas

The governing equation for the unsteady flow of an inviscid compressible gas, written in conservative form, is given by [2]

$$\frac{\partial \boldsymbol{Q}_g}{\partial t} + \frac{\partial \boldsymbol{F}_g}{\partial x} + \frac{\partial \boldsymbol{G}_g}{\partial y} = \boldsymbol{S}_g. \tag{15}$$

The equation of state of an ideal gas is written as

$$p = \rho RT.$$

Equation (15) is complemented by a relation for computing the specific total energy:

$$E = \frac{p}{\gamma - 1} + \frac{1}{2}\rho\left(u_1^2 + u_2^2\right).$$

The vector of conservative variables $\boldsymbol{Q}_g$ and the vectors of flows $\boldsymbol{F}_g$ and $\boldsymbol{G}_g$ have the form

$$\boldsymbol{Q}_g = \begin{pmatrix} \rho \\ \rho u_1 \\ \rho u_2 \\ E \end{pmatrix}, \quad \boldsymbol{F}_g = \begin{pmatrix} \rho u_1 \\ \rho u_1 u_1 + p \\ \rho u_1 u_2 \\ (E+p)u_1 \end{pmatrix}, \quad \boldsymbol{G}_g = \begin{pmatrix} \rho u_2 \\ \rho u_1 u_2 \\ \rho u_2 u_2 + p \\ (E+p)u_2 \end{pmatrix}.$$

Here, t is time, x and y are spatial coordinates, u_1 and u_2 are components of the velocity in the direction of the x and y axes, ρ is density, p is pressure, T is temperature, E is specific total energy, R is gas constant, γ is ratio of specific heat capacities. In dimensionless variables it is assumed that $R = 1/\gamma$ and $\mu = 1/\mathrm{Re}$.

Equation (15) is written in linearized form

$$\frac{\partial \boldsymbol{Q}_g}{\partial t} + A_g \frac{\partial \boldsymbol{Q}_g}{\partial x} + B_g \frac{\partial \boldsymbol{Q}_g}{\partial y} = \boldsymbol{S}_g, \tag{16}$$

where $A_g = \partial \boldsymbol{F}_g / \partial \boldsymbol{Q}_g$ and $B_g = \partial \boldsymbol{G}_g / \partial \boldsymbol{Q}_g$ are Jacobians. In physical variables, Jacobians have the form

$$A_g = \begin{pmatrix} 0 & 1 & 0 & 0 \\ \frac{1}{2}[(\gamma-3)u_1^2+(\gamma-1)u_2^2] & (3-\gamma)u_1 & -(\gamma-1)u_2 & \gamma-1 \\ -u_1u_2 & u_2 & u_1 & 0 \\ -\gamma u_1 E+(\gamma-1)u_1(u_1^2+u_2^2) & \gamma E-\frac{1}{2}(\gamma-1)(3u_1^2+u_2^2) & -(\gamma-1)u_1u_2 & \gamma u_1 \end{pmatrix},$$

$$B_g = \begin{pmatrix} 0 & 0 & 1 & 0 \\ -u_1u_2 & u_2 & u_1 & 0 \\ \frac{1}{2}[(\gamma-1)u_1^2+(\gamma-3)u_2^2] & -(\gamma-1)u_1 & (3-\gamma)u_2 & \gamma-1 \\ -\gamma u_2 E+(\gamma-1)u_2(u_1^2+u_2^2) & -(\gamma-1)u_1u_2 & \gamma E-\frac{1}{2}(\gamma-1)(u_1^2+3u_2^2) & \gamma u_2 \end{pmatrix}.$$

The Jacobian A_g is represented as $A_g = R_g\Lambda_g L_g$, where Λ_g is a diagonal matrix, on the main diagonal of which are the eigenvalues of the Jacobian, L_g and R_g are matrices consisting of the left and right eigenvectors of the Jacobian, and $L_g = R_g^{-1}$. The Jacobian has four real eigenvalues

$$\lambda_1 = u_1 - c, \quad \lambda_2 = u_1, \quad \lambda_3 = u_1, \quad \lambda_4 = u_1 + c.$$

The right eigenvectors of the Jacobian are of the form

$$r_1 = \begin{pmatrix} 1 \\ u_1-c \\ u_2 \\ H-u_1c \end{pmatrix}, \quad r_2 = \begin{pmatrix} 1 \\ u_1 \\ u_2 \\ \frac{1}{2}(u_1^2+u_2^2) \end{pmatrix}, \quad r_3 = \begin{pmatrix} 0 \\ 0 \\ 1 \\ u_2 \end{pmatrix}, \quad r_4 = \begin{pmatrix} 1 \\ u_1+c \\ u_2 \\ H+u_1c \end{pmatrix}.$$

The Jacobian B_g is represented as $B_g = R_g\Lambda_g L_g$, where Λ_g is a diagonal matrix, on the main diagonal of which are the eigenvalues of the Jacobian, L_g and R_g are matrices consisting of the left and right eigenvectors of the Jacobian, and $L_g = R_g^{-1}$. The Jacobian has four real eigenvalues

$$\lambda_1 = u_2 - c, \quad \lambda_2 = u_2, \quad \lambda_3 = u_2, \quad \lambda_4 = u_2 + c.$$

The right eigenvectors of the Jacobian are of the form

$$r_1 = \begin{pmatrix} 1 \\ u_1 \\ u_2-c \\ H-u_2c \end{pmatrix}, \quad r_2 = \begin{pmatrix} 1 \\ u_1 \\ u_2 \\ \frac{1}{2}(u_1^2+u_2^2) \end{pmatrix}, \quad r_3 = \begin{pmatrix} 0 \\ 1 \\ 0 \\ u_1 \end{pmatrix}, \quad r_4 = \begin{pmatrix} 1 \\ u_1 \\ u_2+c \\ H+u_2c \end{pmatrix}.$$

The source term in Equation (15), representing the interphase exchange of momentum and heat, is given by:

$$\boldsymbol{S}_g = \begin{pmatrix} 0 \\ m_p\widetilde{\alpha}(\widetilde{v}_1-u_1)/\tau_v \\ m_p\widetilde{\alpha}(\widetilde{v}_2-u_2)/\tau_v \\ \beta m_p\widetilde{\alpha}(\widetilde{\vartheta}-T)/\tau_\vartheta + m_p\widetilde{\alpha}(\sigma_{11}+\widetilde{v}_1\widetilde{v}_1-u_1\widetilde{v}_1)/\tau_\vartheta + m_p\widetilde{\alpha}(\sigma_{22}+\widetilde{v}_2\widetilde{v}_2-u_2\widetilde{v}_2)/\tau_\vartheta \end{pmatrix}.$$

3.2. Equations of Particles

The governing equation for the motion and heat transfer of the dispersed phase, written in conservative form, is given by:

$$\frac{\partial \boldsymbol{Q}_p}{\partial t} + \frac{\partial \boldsymbol{F}_p}{\partial x} + \frac{\partial \boldsymbol{G}_p}{\partial y} = \boldsymbol{S}_p. \tag{17}$$

The vector of conservative variables $\boldsymbol{Q}_p$ has the form

$$\boldsymbol{Q}_p = \begin{pmatrix} \widetilde{\alpha} \\ \widetilde{\alpha}\widetilde{v}_1 \\ \widetilde{\alpha}\widetilde{v}_2 \\ \widetilde{\alpha}\widetilde{\vartheta} \\ \widetilde{\alpha}(\sigma_{11} + \widetilde{v}_1\widetilde{v}_1) \\ \widetilde{\alpha}(\sigma_{12} + \widetilde{v}_1\widetilde{v}_2) \\ \widetilde{\alpha}(\sigma_{22} + \widetilde{v}_2\widetilde{v}_2) \\ \widetilde{\alpha}(q_1 + \widetilde{v}_1\widetilde{\vartheta}) \\ \widetilde{\alpha}(q_2 + \widetilde{v}_2\widetilde{\vartheta}) \end{pmatrix}.$$

The subgrid stress tensor and subgrid heat flux vector of the dispersed phase are determined from the following relations:

$$\sigma_{ij} = \widetilde{v_i v_j} - \widetilde{v}_i\widetilde{v}_j, \quad q_i = \widetilde{\vartheta v_i} - \widetilde{\vartheta}\widetilde{v}_i.$$

The flow vectors $\boldsymbol{F}_p$ and $\boldsymbol{G}_p$ are expressed through the components of the vector of conservative variables $\boldsymbol{Q}_p = \{Q_i\}$, where $i = 1, \ldots, 9$, and have the form

$$\boldsymbol{F}_p = \begin{pmatrix} Q_2 \\ Q_5 \\ Q_6 \\ Q_8 \\ -Q_1[(2Q_2^3)/Q_1^3 - (3Q_2Q_5)/Q_1^2] \\ Q_1[(2Q_2Q_6)/Q_1^2 + (Q_3Q_5)/Q_1^2 - (2Q_2^2Q_3)/Q_1^3] \\ Q_1[(Q_2Q_7)/Q_1^2 + (2Q_3Q_6)/Q_1^2 - (2Q_2^2Q_3)/Q_1^3] \\ Q_1[(Q_4Q_5)/Q_1^2 + (2Q_2Q_8)/Q_1^2 - (2Q_2^2Q_4)/Q_1^3] \\ Q_1[(Q_4Q_6)/Q_1^2 + (Q_2Q_9)/Q_1^2 + (Q_3Q_8)/Q_1^2 - (2Q_2Q_3Q_4)/Q_1^3] \end{pmatrix},$$

$$\boldsymbol{G}_p = \begin{pmatrix} Q_3 \\ Q_6 \\ Q_7 \\ Q_9 \\ Q_1[(2Q_2Q_6)/Q_1^2 + (Q_3Q_5)/Q_1^2 - (2Q_2^2Q_3)/Q_1^3] \\ Q_1[(Q_2Q_7)/Q_1^2 + (2Q_3Q_6)/Q_1^2 - (2Q_2Q_3^2)/Q_1^3] \\ -Q_1[(2Q_3^3)/Q_1^3 - (3Q_3Q_7)/Q_1^2] \\ Q_1[(Q_4Q_6)/Q_1^2 + (Q_2Q_9)/Q_1^2 + (Q_3Q_8)/Q_1^2 - (2Q_2Q_3Q_4)/Q_1^3] \\ Q_1[(Q_4Q_7)/Q_1^2 + (2Q_3Q_9)/Q_1^2 - (2Q_3^2Q_4)/Q_1^3] \end{pmatrix}.$$

The source term S_p, taking into account the interphase exchange of momentum and heat, has the form

$$\boldsymbol{S}_p = \begin{pmatrix} 0 \\ \widetilde{\alpha}(u_1 - \widetilde{v}_1)/\tau_v \\ \widetilde{\alpha}(u_2 - \widetilde{v}_2)/\tau_v \\ \widetilde{\alpha}(T - \widetilde{\vartheta})/\tau_\vartheta \\ -2\widetilde{\alpha}(\sigma_{11} + \widetilde{v}_1\widetilde{v}_1 - u_1\widetilde{v}_1)/\tau_v \\ -\widetilde{\alpha}(2\sigma_{12} - u_1\widetilde{v}_2 - u_2\widetilde{v}_1 + 2\widetilde{v}_1\widetilde{v}_2)/\tau_v \\ -2\widetilde{\alpha}(\sigma_{22} + \widetilde{v}_2\widetilde{v}_2 - u_2\widetilde{v}_2)/\tau_v \\ -\widetilde{\alpha}(q_1 - T\widetilde{v}_1 + \widetilde{\vartheta}\widetilde{v}_1 + \widetilde{\vartheta}\widetilde{v}_2)/\tau_\vartheta - \widetilde{\alpha}(q_1 - u_1\widetilde{\vartheta} + \widetilde{\vartheta}\widetilde{v}_1 + \widetilde{\vartheta}\widetilde{v}_2)/\tau_v \\ -\widetilde{\alpha}(q_2 - T\widetilde{v}_2 + \widetilde{\vartheta}\widetilde{v}_1 + \widetilde{\vartheta}\widetilde{v}_2)/\tau_\vartheta - \widetilde{\alpha}(q_2 - u_2\widetilde{\vartheta} + \widetilde{\vartheta}\widetilde{v}_1 + \widetilde{\vartheta}\widetilde{v}_2)/\tau_v \end{pmatrix}.$$

Equation (17) describing the motion and heat transfer of the dispersed phase is hyperbolic. In quasi-linear form, Equation (17) takes the form

$$\frac{\partial \boldsymbol{Q}_p}{\partial t} + A_p \frac{\partial \boldsymbol{Q}_p}{\partial x} + B_p \frac{\partial \boldsymbol{Q}_p}{\partial y} = \boldsymbol{S}_p, \tag{18}$$

where $A_p = \partial \boldsymbol{F}_p / \partial \boldsymbol{Q}_p$ and $B_p = \partial \boldsymbol{G}_p / \partial \boldsymbol{Q}_p$ are Jacobians. The Jacobians have the form

$$A_p = \begin{pmatrix} 0 & 1 & 0 & 0 & 0 & 0 & 0 & 0 & 0 \\ 0 & 0 & 0 & 0 & 1 & 0 & 0 & 0 & 0 \\ 0 & 0 & 0 & 0 & 0 & 1 & 0 & 0 & 0 \\ 0 & 0 & 0 & 0 & 0 & 0 & 0 & 1 & 0 \\ \widetilde{v}_1^2 - 3\sigma_{11}\widetilde{v}_1 & 3\sigma_{11} - 3\widetilde{v}_1^2 & 0 & 0 & 3\widetilde{v}_1 & 0 & 0 & 0 & 0 \\ \widetilde{v}_2\widetilde{v}_1^2 - 2\sigma_{12}\widetilde{v}_1 - \sigma_{11}\widetilde{v}_2 & 2\sigma_{12} - 2\widetilde{v}_1\widetilde{v}_2 & \sigma_{11} - \widetilde{v}_1^2 & 0 & \widetilde{v}_2 & 2\widetilde{v}_1 & 0 & 0 & 0 \\ \widetilde{v}_1\widetilde{v}_2^2 - 2\sigma_{12}\widetilde{v}_2 - \sigma_{22}\widetilde{v}_1 & \sigma_{22} - \widetilde{v}_2^2 & 2\sigma_{12} - 2\widetilde{v}_1\widetilde{v}_2 & 0 & 0 & 2\widetilde{v}_2 & \widetilde{v}_1 & 0 & 0 \\ \widetilde{\vartheta}\widetilde{v}_1^2 - 2q_1\widetilde{v}_1 - \sigma_{11}\widetilde{\vartheta} & 2q_1 - 2\widetilde{\vartheta}\widetilde{v}_1 & 0 & \sigma_{11} - \widetilde{v}_1^2 & \widetilde{\vartheta} & 0 & 0 & 2\widetilde{v}_1 & 0 \\ \widetilde{\vartheta}\widetilde{v}_1\widetilde{v}_2 - q_1\widetilde{v}_2 - \sigma_{12}\widetilde{\vartheta} - q_2\widetilde{v}_1 & q_2 - \widetilde{\vartheta}\widetilde{v}_2 & q_1 - \widetilde{\vartheta}\widetilde{v}_1 & \sigma_{12} - \widetilde{v}_1\widetilde{v}_2 & 0 & \widetilde{\vartheta} & 0 & \widetilde{v}_2 & \widetilde{v}_1 \end{pmatrix},$$

$$B_p = \begin{pmatrix} 0 & 0 & 1 & 0 & 0 & 0 & 0 & 0 & 0 \\ 0 & 0 & 0 & 0 & 0 & 1 & 0 & 0 & 0 \\ 0 & 0 & 0 & 0 & 0 & 0 & 1 & 0 & 0 \\ 0 & 0 & 0 & 0 & 0 & 0 & 0 & 0 & 1 \\ \widetilde{v}_2\widetilde{v}_1^2 - 2\sigma_{12}\widetilde{v}_1 - \sigma_{11}\widetilde{v}_2 & 2\sigma_{12} - 2\widetilde{v}_1\widetilde{v}_2 & \sigma_{11} - \widetilde{v}_1^2 & 0 & \widetilde{v}_2 & 2\widetilde{v}_1 & 0 & 0 & 0 \\ \widetilde{v}_1\widetilde{v}_2^2 - 2\sigma_{12}\widetilde{v}_2 - \sigma_{22}\widetilde{v}_1 & \sigma_{22} - \widetilde{v}_2^2 & 2\sigma_{12} - 2\widetilde{v}_1\widetilde{v}_2 & 0 & 0 & 2\widetilde{v}_2 & \widetilde{v}_1 & 0 & 0 \\ \widetilde{v}_2^3 - 3\sigma_{22}\widetilde{v}_2 & 0 & 3\sigma_{22} - 3\widetilde{v}_2^2 & 0 & 0 & 0 & 3\widetilde{v}_2 & 0 & 0 \\ \widetilde{\vartheta}\widetilde{v}_1\widetilde{v}_2 - q_1\widetilde{v}_2 - \sigma_{12}\widetilde{\vartheta} - q_2\widetilde{v}_1 & q_2 - \widetilde{\vartheta}\widetilde{v}_2 & q_1 - \widetilde{\vartheta}\widetilde{v}_1 & \sigma_{12} - \widetilde{v}_1\widetilde{v}_2 & 0 & \widetilde{\vartheta} & 0 & \widetilde{v}_2 & \widetilde{v}_1 \\ \widetilde{\vartheta}\widetilde{v}_2^2 - 2q_2\widetilde{v}_2 - \sigma_{22}\widetilde{\vartheta} & 0 & 2q_2 - 2\widetilde{\vartheta}\widetilde{v}_2 & \sigma_{22} - \widetilde{v}_2^2 & 0 & 0 & \widetilde{\vartheta} & 0 & 2\widetilde{v}_2 \end{pmatrix}.$$

The Jacobian A_p is represented as $A_p = R_p \Lambda_p L_p$, where Λ_p is a diagonal matrix, on the main diagonal of which are the Jacobian eigenvalues, L_p and R_p are matrices consisting of the left and right eigenvectors of the Jacobian, and $L_p = R_p^{-1}$. The Jacobian has nine real eigenvalues

$$\lambda_1 = \widetilde{v}_1 - (3\sigma_{11})^{1/2}, \quad \lambda_2 = \widetilde{v}_1 + (3\sigma_{11})^{1/2}, \quad \lambda_3 = \widetilde{v}_1, \quad \lambda_4 = \widetilde{v}_1, \quad \lambda_5 = \widetilde{v}_1,$$

$$\lambda_6 = \widetilde{v}_1 + \sigma_{11}^{1/2}, \quad \lambda_7 = \widetilde{v}_1 + \sigma_{11}^{1/2}, \quad \lambda_8 = \widetilde{v}_1 - \sigma_{11}^{1/2}, \quad \lambda_9 = \widetilde{v}_1 - \sigma_{11}^{1/2}.$$

The right eigenvectors of the Jacobian are of the form

$$r_1 = \begin{pmatrix} \sigma_{11} \\ \sigma_{11}\widetilde{v}_1 - (3\sigma_{11}^3)^{1/2} \\ \sigma_{11}\widetilde{v}_2 - \sigma_{12}(3\sigma_{11})^{1/2} \\ \sigma_{11}\widetilde{\vartheta} - q_1(3\sigma_{11})^{1/2} \\ \frac{1}{3}\sigma_{11}(3^{1/2}\widetilde{v}_1 - 3\sigma_{11}^{1/2})^2 \\ -\frac{1}{3}\sigma_{11}^{1/2}[3\sigma_{12} - \widetilde{v}_2(3\sigma_{11})^{1/2}](3^{1/2}\widetilde{v}_1 - 3\sigma_{11}^{1/2}) \\ \sigma_{11}\sigma_{22} + \sigma_{11}\widetilde{v}_2^2 + 2\sigma_{12}^2 - 2\widetilde{v}_2\sigma_{12}(3\sigma_{11})^{1/2} \\ -\frac{1}{3}\sigma_{11}^{1/2}[3q_1 - \widetilde{\vartheta}(3\sigma_{11})^{1/2}](3^{1/2}\widetilde{v}_1 - 3\sigma_{11}^{1/2}) \\ 2q_1\sigma_{12} + q_2\sigma_{11} + \sigma_{11}\widetilde{\vartheta}\widetilde{v}_2 - q_1\widetilde{v}_2(3\sigma_{11})^{1/2} - (3\sigma_{11})^{1/2}\sigma_{12}\widetilde{\vartheta} \end{pmatrix},$$

$$r_2 = \begin{pmatrix} \sigma_{11} \\ \sigma_{11}\widetilde{v}_1 + (3\sigma_{11}^3)^{1/2} \\ \sigma_{11}\widetilde{v}_2 + \sigma_{12}(3\sigma_{11})^{1/2} \\ \sigma_{11}\widetilde{\vartheta} + q_1(3\sigma_{11})^{1/2} \\ \frac{1}{3}\sigma_{11}(3^{1/2}\widetilde{v}_1 + 3\sigma_{11}^{1/2})^2 \\ \frac{1}{3}\sigma_{11}^{1/2}[3\sigma_{12} + \widetilde{v}_2(3\sigma_{11})^{1/2}](3^{1/2}\widetilde{v}_1 + 3\sigma_{11}^{1/2}) \\ \sigma_{11}\sigma_{22} + \sigma_{11}\widetilde{v}_2^2 + 2\sigma_{12}^2 + 2\widetilde{v}_2\sigma_{12}(3\sigma_{11})^{1/2} \\ \frac{1}{3}\sigma_{11}^{1/2}[3q_1 + \widetilde{\vartheta}(3\sigma_{11})^{1/2}](3^{1/2}\widetilde{v}_1 + 3\sigma_{11}^{1/2}) \\ 2q_1\sigma_{12} + q_2\sigma_{11} + \sigma_{11}\widetilde{\vartheta}\widetilde{v}_2 + q_1\widetilde{v}_2(3\sigma_{11})^{1/2} + (3\sigma_{11})^{1/2}\sigma_{12}\widetilde{\vartheta} \end{pmatrix},$$

$$r_3 = \begin{pmatrix} 0 \\ 0 \\ 0 \\ 0 \\ 0 \\ 0 \\ 1 \\ 0 \\ 0 \end{pmatrix}, \quad r_4 = \begin{pmatrix} 1 \\ \widetilde{v}_1 \\ \widetilde{v}_2 \\ \widetilde{\vartheta} \\ \widetilde{v}_1^2 \\ \widetilde{v}_1\widetilde{v}_2 \\ 0 \\ \widetilde{\vartheta}\widetilde{v}_1 \\ 0 \end{pmatrix}, \quad r_5 = \begin{pmatrix} 0 \\ 0 \\ 0 \\ 0 \\ 0 \\ 0 \\ 0 \\ 0 \\ 1 \end{pmatrix},$$

$$r_6 = \begin{pmatrix} 0 \\ 0 \\ \sigma_{11}\widetilde{v}_2 + \sigma_{11}^{1/2}\sigma_{12} \\ -\sigma_{11}\widetilde{\vartheta} - q_1\sigma_{11}^{1/2} \\ 0 \\ \sigma_{11}^{1/2}(\sigma_{12} + \sigma_{11}^{1/2}\widetilde{v}_2)(\widetilde{v}_1 + \sigma_{11}^{1/2}) \\ 2(\sigma_{12} + \sigma_{11}^{1/2}\widetilde{v}_2)^2 \\ -\sigma_{11}^{1/2}(q_1 + \sigma_{11}^{1/2}\widetilde{\vartheta})(\widetilde{v}_1 + \sigma_{11}^{1/2}) \\ 0 \end{pmatrix}, \quad r_7 = \begin{pmatrix} 0 \\ 0 \\ \sigma_{11}^{1/2} \\ 0 \\ 0 \\ \sigma_{11} + \widetilde{v}_1\sigma_{11}^{1/2} \\ 2\sigma_{12} + 2\widetilde{v}_2\sigma_{11}^{1/2} \\ 0 \\ q_1 + \widetilde{\vartheta}\sigma_{11}^{1/2} \end{pmatrix},$$

$$r_8 = \begin{pmatrix} 0 \\ 0 \\ \sigma_{11}^{1/2}\sigma_{12} - \sigma_{11}\widetilde{v}_2 \\ \sigma_{11}\widetilde{\vartheta} - q_1\sigma_{11}^{1/2} \\ 0 \\ \sigma_{11}^{1/2}(\widetilde{v}_1 - \sigma_{11}^{1/2})(\sigma_{12} - \sigma_{11}^{1/2}\widetilde{v}_2) \\ -2(\sigma_{12} - \sigma_{11}^{1/2}\widetilde{v}_2)^2 \\ -\sigma_{11}^{1/2}(\widetilde{v}_1 - \sigma_{11}^{1/2})(q_1 - \sigma_{11}^{1/2}\widetilde{\vartheta}) \\ 0 \end{pmatrix}, \quad r_9 = \begin{pmatrix} 0 \\ 0 \\ \sigma_{11}^{1/2} \\ 0 \\ 0 \\ \sigma_{11}^{1/2}\widetilde{v}_1 - \sigma_{11} \\ 2\sigma_{11}\widetilde{v}_2 - 2\sigma_{12} \\ 0 \\ \sigma_{11}^{1/2}\widetilde{\vartheta} - q_1 \end{pmatrix}.$$

The Jacobian B_p is represented as $B_p = R_p\Lambda_p L_p$, where Λ_p is a diagonal matrix, on the main diagonal of which are the eigenvalues of the Jacobian, L_p and R_p are matrices consisting of the left and right eigenvectors of the Jacobian, and $L_p = R_p^{-1}$. The Jacobian has nine real eigenvalues

$$\lambda_1 = \widetilde{v}_2 - (3\sigma_{22})^{1/2}, \quad \lambda_2 = \widetilde{v}_2 + (3\sigma_{22})^{1/2}, \quad \lambda_3 = \widetilde{v}_2, \quad \lambda_4 = \widetilde{v}_2, \quad \lambda_5 = \widetilde{v}_2,$$

$$\lambda_6 = \widetilde{v}_2 + \sigma_{22}^{1/2}, \quad \lambda_7 = \widetilde{v}_2 + \sigma_{22}^{1/2}, \quad \lambda_8 = \widetilde{v}_2 - \sigma_{22}^{1/2}, \quad \lambda_9 = \widetilde{v}_2 - \sigma_{22}^{1/2}.$$

The right eigenvectors of the Jacobian are of the form

$$r_1 = \begin{pmatrix} \sigma_{22} \\ \sigma_{22}\widetilde{v}_1 - \sigma_{12}(3\sigma_{22})^{1/2} \\ \sigma_{22}\widetilde{v}_2 - (3\sigma_{22}^3)^{1/2} \\ \sigma_{22}\widetilde{\vartheta} - q_2(3\sigma_{22})^{1/2} \\ \sigma_{11}\sigma_{22} + \sigma_{22}\widetilde{v}_1^2 + 2\sigma_{12}^2 - 2\widetilde{v}_1\sigma_{12}(3\sigma_{22})^{1/2} \\ -\frac{1}{3}\sigma_{22}^{1/2}[3\sigma_{12} - \widetilde{v}_1(3\sigma_{22})^{1/2}](3^{1/2}\widetilde{v}_2 - 3\sigma_{22}^{1/2}) \\ \frac{1}{3}\sigma_{22}(3^{1/2}\widetilde{v}_2 - 3\sigma_{22}^{1/2})^2 \\ 2q_2\sigma_{12} + q_1\sigma_{22} + \sigma_{22}\widetilde{\vartheta}\widetilde{v}_1 - q_2\widetilde{v}_1(3\sigma_{22})^{1/2} - \sigma_{12}\widetilde{\vartheta}(3\sigma_{22})^{1/2} \\ -\frac{1}{3}\sigma_{22}^{1/2}[3q_2 - \widetilde{\vartheta}(3\sigma_{22})^{1/2}](3^{1/2}\widetilde{v}_2 - 3\sigma_{22}^{1/2}) \end{pmatrix},$$

$$r_2 = \begin{pmatrix} \sigma_{22} \\ \sigma_{22}\widetilde{v}_1 + \sigma_{12}(3\sigma_{22})^{1/2} \\ \sigma_{22}\widetilde{v}_2 + (3\sigma_{22}^3)^{1/2} \\ \sigma_{22}\widetilde{\vartheta} + q_2(3\sigma_{22})^{1/2} \\ \sigma_{11}\sigma_{22} + \sigma_{22}\widetilde{v}_1^2 + 2\sigma_{12}^2 + 2\widetilde{v}_1\sigma_{12}(3\sigma_{22})^{1/2} \\ \frac{1}{3}\sigma_{22}^{1/2}[3\sigma_{12} + \widetilde{v}_1(3\sigma_{22})^{1/2}](3^{1/2}\widetilde{v}_2 + 3\sigma_{22}^{1/2}) \\ \frac{1}{3}\sigma_{22}(3^{1/2}\widetilde{v}_2 + 3\sigma_{22}^{1/2})^2 \\ 2q_2\sigma_{12} + q_1\sigma_{22} + \sigma_{22}\widetilde{\vartheta}\widetilde{v}_1 + q_2\widetilde{v}_1(3\sigma_{22})^{1/2} + \sigma_{12}\widetilde{\vartheta}(3\sigma_{22})^{1/2} \\ \frac{1}{3}\sigma_{22}^{1/2}[3q_2 + \widetilde{\vartheta}(3\sigma_{22})^{1/2}](3^{1/2}\widetilde{v}_2 + 3\sigma_{22}^{1/2}) \end{pmatrix},$$

$$r_3 = \begin{pmatrix} 0 \\ 0 \\ 0 \\ 0 \\ 1 \\ 0 \\ 0 \\ 0 \\ 0 \end{pmatrix}, \quad r_4 = \begin{pmatrix} 0 \\ 0 \\ 0 \\ 0 \\ 0 \\ 0 \\ 0 \\ 1 \\ 0 \end{pmatrix}, \quad r_5 = \begin{pmatrix} 1 \\ \widetilde{v}_1 \\ \widetilde{v}_2 \\ \widetilde{\vartheta} \\ 0 \\ \widetilde{v}_1\widetilde{v}_2 \\ \widetilde{v}_2^2 \\ 0 \\ \widetilde{\vartheta}\widetilde{v}_2 \end{pmatrix},$$

$$r_6 = \begin{pmatrix} 0 \\ \sigma_{22}^{1/2} \\ 0 \\ 0 \\ 2\sigma_{12} + 2\widetilde{v}_1\sigma_{22}^{1/2} \\ \sigma_{22} + \widetilde{v}_2\sigma_{22}^{1/2} \\ 0 \\ q_2 + \widetilde{\vartheta}\sigma_{22}^{1/2} \\ 0 \end{pmatrix}, \quad r_7 = \begin{pmatrix} 0 \\ \sigma_{22}\widetilde{v}_1 + \sigma_{22}^{1/2}\sigma_{12} \\ 0 \\ -\sigma_{22}\widetilde{\vartheta} - q_2\sigma_{22}^{1/2} \\ 2(\sigma_{12} + \sigma_{22}^{1/2}\widetilde{v}_1)^2 \\ \sigma_{22}^{1/2}(\sigma_{12} + \sigma_{22}^{1/2}\widetilde{v}_1)(\widetilde{v}_2 + \sigma_{22}^{1/2}) \\ 0 \\ 0 \\ -\sigma_{22}^{1/2}(q_2 + \sigma_{22}^{1/2}\widetilde{\vartheta})(\widetilde{v}_2 + \sigma_{22}^{1/2}) \end{pmatrix},$$

$$r_8 = \begin{pmatrix} 0 \\ \sigma_{22}^{1/2} \\ 0 \\ 0 \\ 2\sigma_{22}^{1/2}\widetilde{v}_1 - 2\sigma_{12} \\ \sigma_{22}\widetilde{v}_2 - \sigma_{22} \\ 0 \\ \sigma_{22}^{1/2}\widetilde{\vartheta} - q_2 \\ 0 \end{pmatrix}, \quad r_9 = \begin{pmatrix} 0 \\ \sigma_{22}^{1/2}\sigma_{12} - \sigma_{22}\widetilde{v}_1 \\ 0 \\ \sigma_{22}\widetilde{\vartheta} - q_2\sigma_{22}^{1/2} \\ -2(\sigma_{12} - \sigma_{22}^{1/2}\widetilde{v}_1)^2 \\ \sigma_{22}^{1/2}(\widetilde{v}_2 - \sigma_{22}^{1/2})(\sigma_{12} - \sigma_{22}^{1/2}\widetilde{v}_1) \\ 0 \\ 0 \\ -\sigma_{22}^{1/2}(\widetilde{v}_2 - \sigma_{22}^{1/2})(q_2 - \sigma_{22}^{1/2}\widetilde{\vartheta}) \end{pmatrix}.$$

The Jacobian eigenvalues of the dispersed phase depend on the velocity components (v_1 and v_2) and the subgrid stress tensor components (σ_{11} and σ_{22}). At certain points in time, the matrices formed from the Jacobian eigenvectors may become singular. This occurs, for example, when $\widetilde{v}_1 = 0$ or $\widetilde{v}_2 = 0$ or $\sigma_{11} = 0$ or $\sigma_{22} = 0$. The subgrid stresses of the dispersed phase σ_{11} and σ_{22} vanish in a uniform flow when the particle velocity differs only slightly from that of the gas. To prevent singularities in regions of the flow where particles are absent, the subgrid stresses of the dispersed phase are assigned a small positive value, $\varepsilon = 10^{-3}$.

4. Numerical Method

The finite volume method is employed to discretize the governing equations, with the Godunov method used to compute fluxes across the faces of the control volumes [39]. Temporal discretization is performed using a third-order Runge–Kutta method. A dimensional splitting approach is applied to extend the computational procedure to two dimensions. On each face of a control volume, the Riemann problem for the decay of an arbitrary discontinuity is solved.

4.1. Numerical Schemes

The presence of strong discontinuities and regions with steep gradients in flow parameters (shock waves, contact discontinuities) necessitates the use of numerical methods capable of accurately capturing both qualitative and quantitative features of the flow [4].

High-order numerical methods for computational fluid dynamics (CFD) problems with discontinuous solutions build upon the classical first-order method developed for the decay of an arbitrary discontinuity [40]. Higher-order accuracy is achieved through polynomial reconstructions of gas-dynamic variables and the application of limiter functions, as in TVD schemes. In ENO schemes, an interpolation polynomial is used to compute variables at cell faces, with the polynomial chosen from several candidates based on local smoothness. The order of the scheme depends on the number of candidate polynomials considered. WENO schemes extend this approach by taking a weighted combination of all

possible polynomials for each cell, rather than selecting a single one as in ENO schemes. In practice, ENO- and WENO-based schemes provide non-oscillatory solutions near discontinuities at arbitrary orders of approximation. Various modifications of TVD, ENO, and WENO schemes, often combined with Runge–Kutta methods for time integration, are widely employed in practical simulations [4].

A review of numerical methods for modeling shock-wave and detonation processes in gas–dispersed mixtures is presented in [41].

For simulating supersonic flows of pure gas, Godunov-type schemes [29,42–46] and schemes based on the separation of discontinuities [47,48] are widely employed. In turbulent flows, the parabolic components of the equations are often solved using implicit methods [44,49]. In several studies, Godunov schemes have also been successfully applied to the discrete phase [44,45,50], with the gas and particle equations formulated in conservative form and the pressure proportional to the volume fraction of each phase. Calculations of both phases using general finite-difference methods have been carried out in [51] (large-particle method), [52] (finite element method), and [53] (McCormack scheme).

Flux-corrected transport (FCT) schemes have been applied to simulate both gas flow [52–54] and particle motion [43,46]. TVD-type schemes, which employ monotonizing operators, are used for the gas phase in [55,56], and monotonizing corrections are also implemented in [45,50].

For gas–suspension dynamics at low dispersed-phase concentrations, the governing equations for particle motion do not include pressure. As a result, applying TVD schemes to the solid-phase equations is limited by the degeneracy of the Jacobian eigenvector space, since the particle equations are not strictly hyperbolic. Specifically, for the discrete-phase part of the Jacobian, the eigenvalue $\lambda = u_p$ has multiplicity three, yielding two eigenvectors and one associated vector. The particle equations, however, resemble a vortex transport equation and, thus, numerical methods developed for the vortex equation—such as the McCormack scheme and the upstream-difference scheme proposed by Gentry [57] (Gentry–Martin–Daly)—are used for their solution.

The numerical methods developed for supersonic gas flows are not always directly applicable to the discrete phase at low particle volume concentrations, where the particle volume is neglected, due to the degeneracy of the equations governing particle evolution. This degeneracy arises from the absence of a term corresponding to the total pressure of the mixture in the discrete-phase equations. The large-particle method is applied in [47], while the McCormack scheme is used to compute the particle subsystem in [43,46,55,56]. In [58], the Gentry–Martin–Daly scheme, a flow-upwind difference scheme [57], is employed to calculate both the dynamics and thermal history of particles.

The contact discontinuity of the dispersed phase is treated in [59] as a thin layer across which gas parameters vary continuously, with all necessary derivatives well-defined. Thin-layer equations are derived to relate the medium parameters on either side of the contact discontinuity, and a solution approach for these equations is proposed.

To improve computational efficiency, moving or adaptive grids are employed to enhance the resolution of shock waves [44,52], and parallel computing techniques are applied [41,50]. Methods for adapting TVD schemes to simulate finely dispersed gas suspensions (within the single-velocity, two-temperature model) and ultra-dispersed gas suspensions are presented in [41]. The compressible-phase equations are solved using an explicit finite-difference TVD scheme, which provides high accuracy in resolving strong discontinuities on a standard stencil, eliminates spurious oscillations behind shock fronts typical of dispersive schemes, and ensures stability when the Courant–Friedrichs–Lewy (CFL) condition is satisfied. The use of TVD schemes is also justified for flows with sharp variations in flow parameters.

Finite-difference WENO schemes of third- and fifth-order accuracy (including the WENO-Z scheme) are employed in [60,61] for modeling compressible gas flows with particles, using a mixed Eulerian–Lagrangian approach. Spatial discretization is performed on a uniform mesh, while time integration uses a third-order Runge–Kutta method. In [29], results obtained with different difference schemes (Godunov and WENO) are compared with data computed using Eulerian and Lagrangian descriptions of the dispersed phase for one-dimensional simulations of shock-wave interactions with a particle cloud. Accounting for the volume occupied by particles ensures hyperbolicity of the equations governing the dynamics and heat transfer of the dispersed phase, enabling the application of the Godunov method to discretize both the gas and particle equations.

For gas suspensions containing small reacting particles, the scales of phase-velocity relaxation are neglected, and a single-velocity, two-temperature approximation of heterogeneous media mechanics is adopted [62]. A modified TVD scheme, based on the method proposed in [63] for a non-ideal gas, is used to solve the equations. This scheme has been successfully applied to simulate detonation flows in gas suspensions of aluminum particles, as well as coal dust [41,58]. The governing equations for the mixture as a whole are solved in Eulerian variables, while the equations describing thermal and chemical relaxation are integrated in Lagrangian variables. Schemes based on the exact solution of the Riemann problem for multi-component media, which ensure monotonicity and positivity of phase mass concentrations, are proposed in [64,65]. These schemes prevent oscillations in the pressure distribution at contact boundaries and are capable of accurately capturing strong discontinuous fronts.

In ultra-dispersed mixtures, the lengths of the velocity- and thermal-relaxation zones are several orders of magnitude smaller than the characteristic scales of the problem and the scales over which the dispersed-phase mass concentration changes. To model processes at the macroscale, the gas–particle mixture is assumed to be in equilibrium in velocity and temperature, while remaining non-equilibrium in chemical composition.

Numerical modeling of detonation processes in two-phase mixtures requires extensive simulations. TVD schemes, which are widely used, improve the accuracy of the numerical solution at shock fronts but involve a large number of logical operations. One way to increase computational efficiency, in addition to using adaptive grids, is the application of multiprocessor computing systems.

To simplify the numerical implementation of two-phase flow calculations, an approach is employed that allows the equations for the gas and dispersed phases to be formulated with a similar hyperbolic structure.

4.2. Finite Volume Method

A uniform mesh consisting of $N \times N$ cells is considered. Cell centers are located at the points $x_i = i\Delta x$ and $y_j = j\Delta y$, where $i, j = 0, 1, \ldots, N$. The vector of conservative variables averaged over the cell $[x_{i-1/2}, x_{i+1/2}] \times [y_{i-1/2}, y_{i+1/2}]$ is determined by the relation

$$\boldsymbol{Q}_{i,j} = \frac{1}{\Delta x_i \Delta y_j} \int_{x_{i-1/2}}^{x_{i+1/2}} \int_{y_{j-1/2}}^{y_{j+1/2}} \boldsymbol{Q} dx dy,$$

where $\Delta x = x_{i+1/2} - x_{i-1/2}$ and $\Delta y = y_{j+1/2} - y_{j-1/2}$. In discrete form, the Equation (15) is written as follows:

— in x direction

$$\boldsymbol{Q}^*_{i,j} = \boldsymbol{Q}^n_{i,j} - \frac{\Delta t}{\Delta x}\left(\boldsymbol{F}^n_{i+1/2,j} - \boldsymbol{F}^n_{i-1/2,j}\right) + \Delta t \boldsymbol{S}_x; \tag{19}$$

— in y direction

$$\boldsymbol{Q}_{i,j}^{n+1} = \boldsymbol{Q}_{i,j}^{*} - \frac{\Delta t}{\Delta y}\left(\boldsymbol{G}_{i,j+1/2}^{n} - \boldsymbol{G}_{i,j-1/2}^{n}\right) + \Delta t \boldsymbol{S}_{y}; \tag{20}$$

The integration step over time is selected based on the condition

$$\Delta t = \mathrm{CFL}\frac{\min\{\Delta x, \Delta y\}}{\max\{|\lambda_{gi}|, |\lambda_{pi}|\}},$$

where $\mathrm{CFL} \leqslant 1/2$.

Using flux vector splitting, the Jacobian is represented as $A = R(\Lambda^{+} + \Lambda^{-})R^{-1}$, where Λ^{+} and Λ^{-} are diagonal matrices with positive and negative eigenvalues on the main diagonal. The fluxes are found from the relations

$$\boldsymbol{F}_{i-1/2,j} = A^{+}\boldsymbol{Q}_{i-1,j} + A^{-}\boldsymbol{Q}_{i,j};$$
$$\boldsymbol{G}_{i,j-1/2} = B^{+}\boldsymbol{Q}_{i,j-1} + B^{-}\boldsymbol{Q}_{i,j}.$$

The components of the matrices A^{+}, A^{-} and B^{+}, B^{-} are found using Roe-averaged values.

The source term in the Equation (15) is represented in the split form $\boldsymbol{S}_{g} = \boldsymbol{S}_{gx} + \boldsymbol{S}_{gy}$. The source terms in the x and y directions are of the form

— in x direction

$$\boldsymbol{S}_{gx} = \begin{pmatrix} 0 \\ m_p\widetilde{\alpha}(\widetilde{v}_1 - u_1)/\tau_v \\ 0 \\ \beta m_p\widetilde{\alpha}(\widetilde{\vartheta} - T)/\tau_\vartheta + m_p\widetilde{\alpha}(\sigma_{11} + \widetilde{v}_1^2 - u_1\widetilde{v}_1)/\tau_\vartheta \end{pmatrix};$$

— in y direction

$$\boldsymbol{S}_{gy} = \begin{pmatrix} 0 \\ 0 \\ m_p\widetilde{\alpha}(\widetilde{v}_2 - u_2)/\tau_v \\ m_p\widetilde{\alpha}(\sigma_{22} + \widetilde{v}_2^2 - u_2\widetilde{v}_2)/\tau_\vartheta \end{pmatrix}.$$

The source term in Equation (17) is also represented in split form $\boldsymbol{S}_{p} = \boldsymbol{S}_{px} + \boldsymbol{S}_{py}$. The source terms in the directions of the x and y axes have the form

— in x direction

$$\boldsymbol{S}_{px} = \begin{pmatrix} 0 \\ \widetilde{\alpha}(u_1 - \widetilde{v}_1)/\tau_v \\ 0 \\ \widetilde{\alpha}(T - \widetilde{\vartheta})/\tau_\vartheta \\ -2\widetilde{\alpha}(\sigma_{11} + \widetilde{v}_1^2 - u_1\widetilde{v}_1)/\tau_v \\ -\widetilde{\alpha}(\sigma_{12} - u_2\widetilde{v}_1 + \widetilde{v}_1\widetilde{v}_2)/\tau_v \\ 0 \\ -\widetilde{\alpha}(q_1 - T\widetilde{v}_1 + \widetilde{\vartheta}\widetilde{v}_1 + \widetilde{\vartheta}\widetilde{v}_2)/\tau_\vartheta - \widetilde{\alpha}(q_1 - u_1\widetilde{\vartheta} + \widetilde{\vartheta}\widetilde{v}_1 + \widetilde{\vartheta}\widetilde{v}_2)/\tau_v \\ 0 \end{pmatrix};$$

— in y direction

$$\boldsymbol{S}_{py} = \begin{pmatrix} 0 \\ 0 \\ \widetilde{\alpha}(u_2 - \widetilde{v}_2)/\tau_v \\ 0 \\ 0 \\ -\widetilde{\alpha}(\sigma_{12} - u_1\widetilde{v}_2 + \widetilde{v}_1\widetilde{v}_2)/\tau_v \\ -2\widetilde{\alpha}(\sigma_{22} + \widetilde{v}_2^2 - u_2\widetilde{v}_2)/\tau_v \\ 0 \\ -\widetilde{\alpha}(q_2 - T\widetilde{v}_2 + \widetilde{\vartheta}\widetilde{v}_1 + \widetilde{\vartheta}\widetilde{v}_2)/\tau_\vartheta - \widetilde{\alpha}(q_2 - u_2\widetilde{\vartheta} + \widetilde{\vartheta}\widetilde{v}_1 + \widetilde{\vartheta}\widetilde{v}_2)/\tau_v \end{pmatrix}.$$

For the gas phase, Roe averaging is given by the following relations

$$\widehat{u}_{i-1/2} = \frac{\rho_{i-1}^{1/2}u_{i-1} + \rho_i^{1/2}u_i}{\rho_{i-1}^{1/2} + \rho_i^{1/2}};$$
$$\widehat{v}_{i-1/2} = \frac{\rho_{i-1}^{1/2}v_{i-1} + \rho_i^{1/2}v_i}{\rho_{i-1}^{1/2} + \rho_i^{1/2}};$$
$$\widehat{H}_{i-1/2} = \frac{\rho_{i-1}^{1/2}H_{i-1} + \rho_i^{1/2}H_i}{\rho_{i-1}^{1/2} + \rho_i^{1/2}} = \frac{(E_{i-1} + p_{i-1})/\rho_{i-1}^{1/2} + (E_i + p_i)/\rho_i^{1/2}}{\rho_{i-1}^{1/2} + \rho_i^{1/2}}.$$

The local speed of sound is found from the relation

$$\widehat{c} = \left\{(\gamma - 1)\left[\widehat{H} - \frac{1}{2}\left(\widehat{u}^2 + \widehat{v}^2\right)\right]\right\}^{1/2},$$

where H is total enthalpy.

For the dispersed phase, averaging is given by the following relations

$$\widehat{q}_{i-1/2} = \frac{1}{2}(q_{i-1} + q_i),$$

where q is flow variable ($q = \widetilde{\alpha}$, $\widetilde{v}_i$, $\widetilde{\vartheta}$, $\widetilde{v_i v_j}$, $\widetilde{\vartheta v_i}$).

The longitudinal dimension of the computational domain is several times—often an order of magnitude—larger than the transverse dimension. To parallelize the calculations, the domain is decomposed linearly along the x-coordinate, with each subdomain assigned to a separate processor. The array size is constrained by the number of points handled by each processor. Calculations at each time step are performed simultaneously on all processors, with data exchanged between processors at every time step [4].

At the inlet boundary, a prescribed incident shock wave is imposed using the Rankine–Hugoniot relations for a given Mach number. The post-shock pressure, density and velocity are set to constant values corresponding to the shock conditions, while pre-shock conditions represent the undisturbed gas phase. The right boundary is treated as a non-reflecting (open) boundary, implemented using a characteristic-based formulation that allows outgoing waves to exit the computational domain without artificial reflection. The upper and lower boundaries are set as symmetry boundaries, assuming the shock-particle interaction zone is laterally uniform over the region of interest.

The domain is initially filled with a uniform gas at rest, with a specified distribution of solid particles characterized by volume fraction, particle diameter, and material density. The shock wave is initialized at a prescribed distance upstream of the particle cloud interface.

5. Results and Discussion

The interaction of a shock wave with Mach number 3 with a rectangular particle cloud is considered (Figure 1). The computational domain is a rectangle of length L and height H in the Cartesian coordinate system (x, y), filled with air initially at rest under normal conditions. At the left boundary, inflow conditions for air ($\gamma = 1.4$) are specified, corresponding to the post-shock parameters for a shock wave of the given Mach number (M = 3). No-flow (wall) boundary conditions are applied at all other boundaries. During the simulation, the transmitted and reflected waves do not reach the domain boundaries. The volume concentration of the dispersed phase is calculated as $\varkappa = \pi N D^2/(4LH)$, where N is the number of particles in a square cloud of area $L \times H$, and D is the particle diameter.

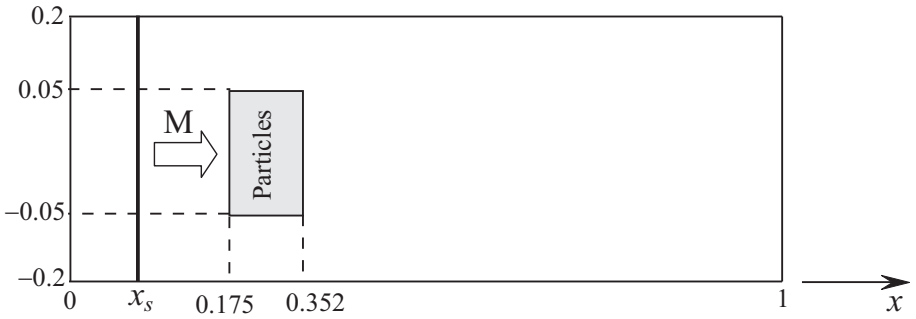


Figure 1. Interaction of a shock wave with a rectangular particle cloud. Arrow shows direction of incoming flow.

At the initial moment, the shock wave front is located at $x_s = 0.0175$ in the rectangular domain $[0, 1] \times [-0.2, 0.2]$. Behind the shock wave, the gas is at rest ($u_1 = u_2 = 0$), with density and pressure set to $\rho = 1$ and $p = 1$. Particles with density $\rho_p = 1000$ kg/m^3 and diameter $d_p = 5.86 \times 10^{-3}$ m are uniformly distributed in the region $[0.175, 0.352] \times [-0.05, 0.05]$. The cloud consists of 4×10^4 particles, corresponding to a particle number concentration of $\widetilde{\varkappa} = 2.26 \times 10^6$ m^{-3}. The Stokes number is set to Stk = 1, and the ratio of the specific heat capacities of the gas and particles is $\beta = 0.4$. The Prandtl number is assigned the value Pr = 0.72. At $t = 0$, the particles are assumed to be at rest ($\widetilde{v}_1 = \widetilde{v}_2 = 0$), with temperature equal to the gas temperature ($\widetilde{\vartheta} = T_g$). The correlation moments associated with the dispersed phase are initially set to zero ($\sigma_{ij} = 0, q_i = 0$).

If an incident shock with Mach number M = 3, the post-shock flow velocity is not zero in the laboratory frame when the upstream gas is initially at rest. In numerical studies or shock–particle interaction models, the reference frame is changed to simplify the setup. In the shock-fixed frame, the shock is stationary, and the post-shock gas appears stationary ($u_2 = 0$) because the coordinate system moves with the shock front.

The calculations are performed on a grid of 1500×500 nodes up to time $t_f = 0.12$, by which point the shock wave has passed through the region occupied by the particles. The particle cloud itself is resolved on a grid block of 200×200 nodes.

A mesh refinement study has been conducted for the two-dimensional simulations. The results show that the pressure peak and shock-front position vary by less than 3% between the two finest meshes, confirming that the solution is mesh-independent within this tolerance.

For a fixed intensity of the incident shock wave, the key parameters of the problem are the permeability S of the particle system, its length L, and the particle diameter D. The permeability of the backfill, S, is defined as the ratio of the area occupied by the gas within the backfill volume to the total backfill area $S = 1 - N\pi D^2/(4LH)$, where N is the number of particles and H is the cloud height. This definition is consistent with that given in [9].

The distribution of the carrier flow characteristics at time $t = 0.1$ is shown in Figure 2. The gas velocity in the y-direction remains relatively small. Near the left boundary of the particle cloud, a sharp jump in the flow parameters is observed, characterized by an increase in density, pressure, and temperature, accompanied by a decrease in velocity and Mach number.

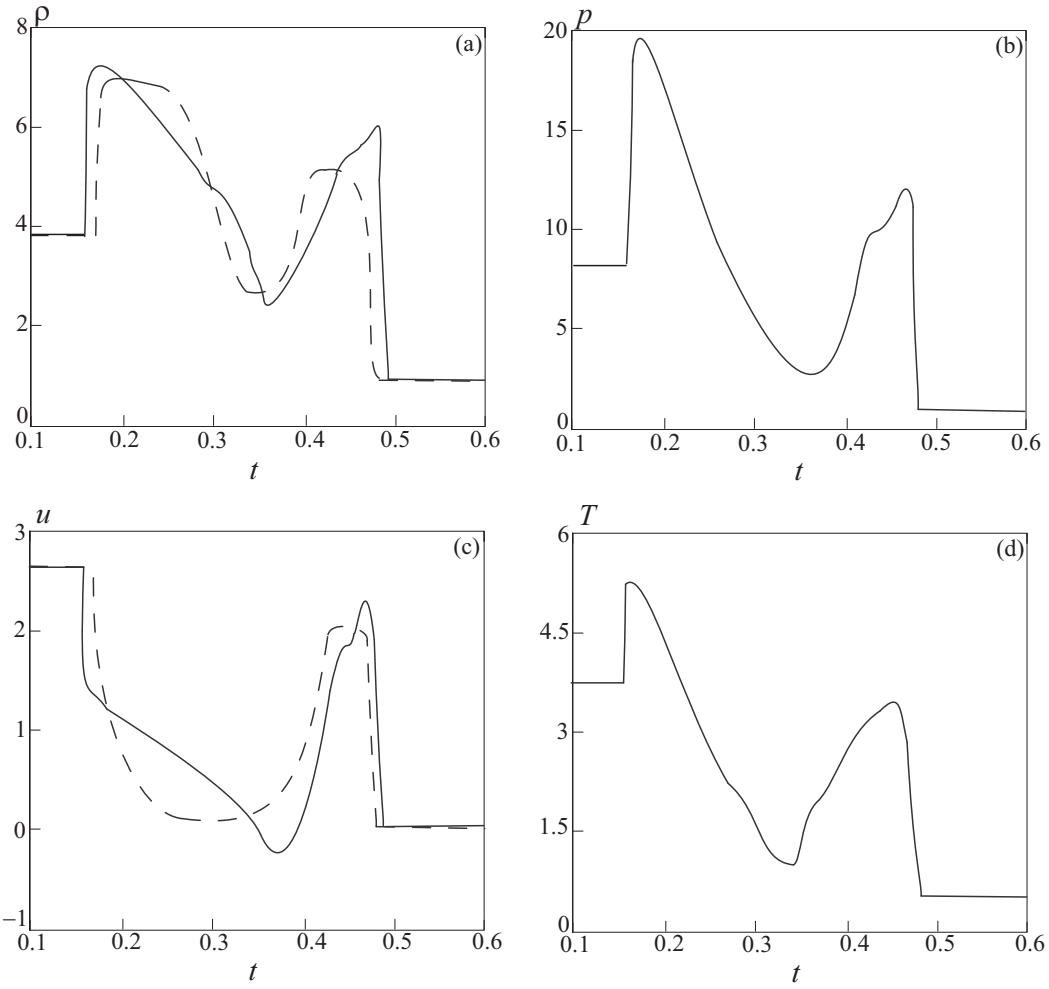


Figure 2. Distributions of density (**a**), pressure (**b**), velocity (**c**), and temperature (**d**) at $y = 0$ at time $t = 0.1$ (solid lines). Dashed lines show the distributions of flow characteristics corresponding to the one-dimensional calculation.

Qualitative agreement between the one-dimensional and two-dimensional formulations does not in itself demonstrate the physical accuracy of the results. The purpose in comparing the two formulations was to verify the numerical consistency of the solution approaches and to assess the influence of dimensionality under identical modeling assumptions (e.g., uniform particle volume fraction, inviscid carrier phase, and equilibrium drag formulation). While detailed experimental data for the specific configuration considered are not currently available, the results computed were compared with published data on shock attenuation and pressure decay in particle-laden flows. The observed trends and magnitudes of pressure reduction are consistent with experimental studies [23], supporting the physical plausibility of the numerical predictions [31].

Comparison of the pressure distributions obtained in the one-dimensional and two-dimensional formulations (Figure 2, solid and dashed lines) shows that the overall shock-wave flow pattern is similar in both cases. However, in the two-dimensional calculation, the reflected shock wave is more intense than in the one-dimensional case, and the pressure

maximum (corresponding to the front of the reflected shock wave) is located closer to the left boundary of the particle cloud. Additionally, the pressure decrease in the one-dimensional case occurs more rapidly than in the two-dimensional calculation. Near the right boundary of the cloud, a flow expansion region is observed, which is less pronounced in the one-dimensional case. The reflected shock wave is relatively weak, resulting in a region of slightly elevated pressure behind the right boundary of the cloud.

The level lines of the carrier flow characteristics are shown in Figures 3 and 4. At the point where the shock wave contacts the particle cloud, a sharp jump in density is observed. The head shock wave front symmetrically envelops the region occupied by the particles. Behind the particle cloud, a Mach reflection of the shock wave occurs from the axis of symmetry, accompanied by a recirculation region similar to that observed in flows around blunt bodies.

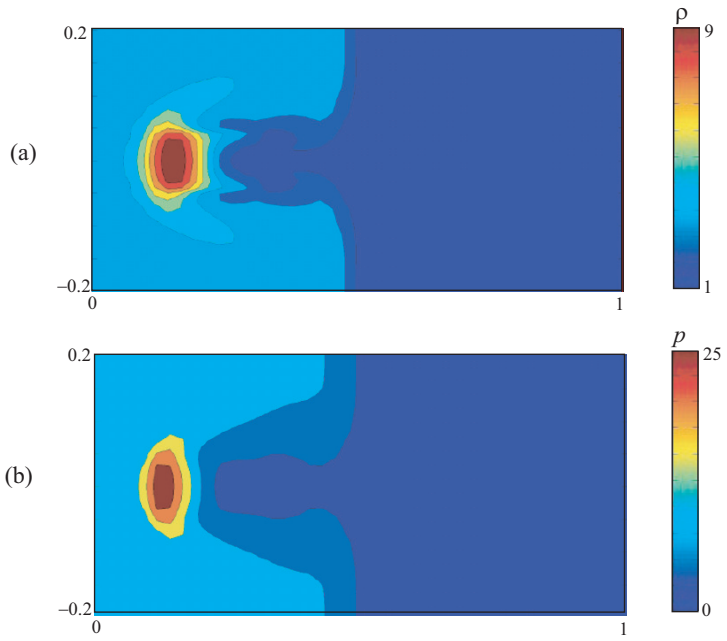


Figure 3. Contours of the density (**a**) and pressure (**b**) of gas at time $t = 0.1$.

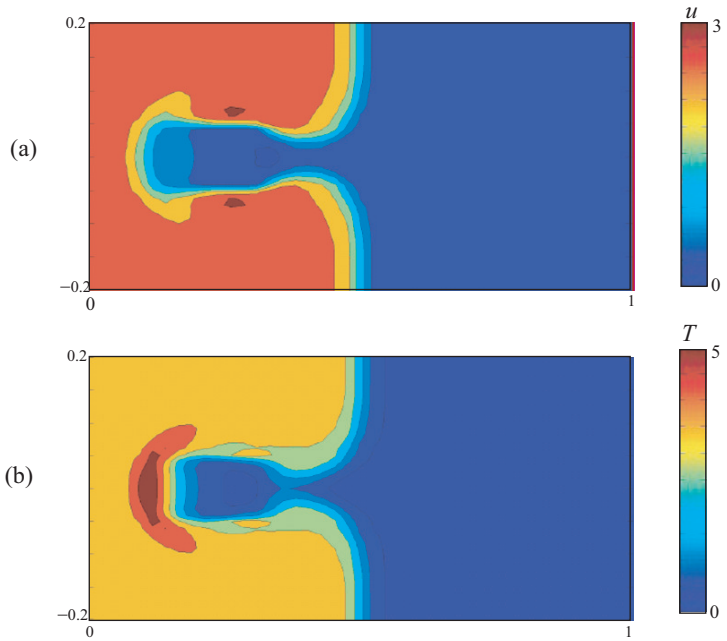


Figure 4. Contours of the velocity (**a**) and temperature (**b**) of gas at time $t = 0.1$.

The velocity and temperature distributions of the dispersed phase are shown in Figure 5. Both velocity and temperature exhibit a monotonic decrease from the left to the right boundary of the cloud. The pressure and density distributions follow a similar pattern to the velocity profile. Near the left boundary of the cloud, the flow characteristics change rapidly, followed by a more gradual, nearly linear decrease within the region occupied by the particles.

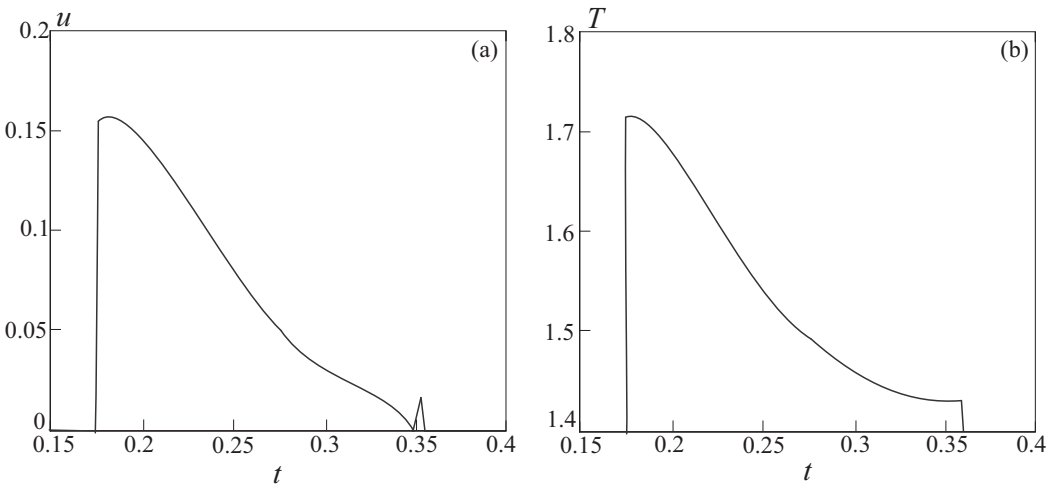


Figure 5. Distributions of velocity (**a**) and temperature (**b**) of the dispersed phase at $y = 0$ at time $t = 0.1$.

The concentration levels and velocity lines of the dispersed phase are shown in Figure 6. The interaction of the shock wave with the particle cloud sets the particles in motion, causing the left boundary of the cloud to become diffuse. The velocity of the dispersed phase at the edges of the cloud is higher than that of the particles near the center of its left boundary. Behind the cloud, a recirculation region forms, where the particles remain essentially stationary and do not interact with the gas flow. The left boundary of the cloud moves from left to right and becomes blurred along both directions of the y-axis. At the right boundary, only the particles near the cloud edges acquire a non-zero velocity directed inward and toward the exit boundary.

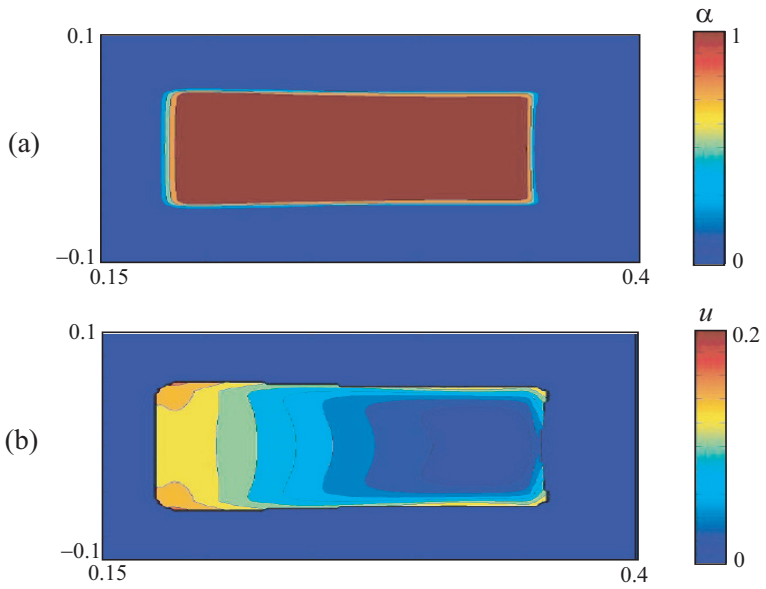


Figure 6. Contours of concentration (**a**) and velocity (**b**) of the dispersed phase at time $t = 0.1$.

The nearly uniform dispersed-phase concentration within the particle cloud results from the short duration of the shock–particle interaction relative to the characteristic time for particle redistribution. Large particle inertia prevents rapid rearrangement. The particles possess much greater density than the carrier gas (often by 3–4 orders of magnitude). As a result, their response time is large compared to the gas flow time scale across the cloud. Consequently, during the short shock-passage period, particles do not have sufficient time to accelerate or separate significantly from one another.

Small interphase velocity slip in dense configurations. In regions of high particle concentration (volume fraction near unity), strong drag coupling between neighbouring particles and the gas phase suppresses large local velocity gradients. This coupling maintains a nearly homogeneous particle distribution, especially in the early stages following shock impact. Negligible volumetric expansion of the solid phase. Unlike the gas, the solid phase is effectively incompressible under the considered conditions, so the particle volume fraction remains almost constant, even though the gas phase undergoes sharp compression and relaxation.

The dispersed-phase concentration remains essentially constant and close to its initial value because the shock interaction time is too short for significant particle rearrangement, the particles are strongly inertia-dominated, and the model treats the particulate phase as a continuous field without resolving sub-grid-scale clustering.

The results obtained from two-dimensional calculations, averaged over the transverse direction, and from the one-dimensional model are qualitatively similar. In the two-dimensional case, the cross-section-averaged pressure from the right edge of the cloud up to the contact discontinuity is lower than in the one-dimensional calculation. The positions of the fronts of the reflected and transmitted shock waves obtained from both models are in good agreement. However, the one-dimensional model does not capture the fluctuations in flow parameters observed in the two-dimensional calculations.

When the backfill density (or equivalently, when the permeability decreases), the resistance to gas motion within the particle layer increases, altering both the reflected and transmitted shock characteristics. For denser backfills, the impedance contrast at the front interface is larger, leading to a stronger reflected shock and a higher reflected-wave velocity. At the same time, the transmitted wave entering the backfill experiences stronger attenuation due to enhanced drag and energy dissipation, resulting in a weaker transmitted front and a more smeared pressure profile.

The reduced permeability intensifies gas–particle momentum coupling, which suppresses large-scale flow divergence and, therefore, makes multidimensional effects less pronounced in the reflected-wave region. Conversely, behind the transmitted shock, the turbulent wake becomes more developed as interphase interactions generate unsteady vortices and local fluctuations in particle concentration.

The smooth pressure rise to the mean post-interaction level, following the initial jump, originates from multiple reflections and difractions of the leading shock by individual particles, as well as from multidimensional flow effects that cannot be captured by one-dimensional formulations [30]. After the transmitted wave passes through the backfill, the flow parameters approach a quasi-stationary state with oscillations caused by vortex shedding and recirculation in the particle wake region.

Parametric calculations reveal that increasing the backfill length or decreasing particle diameter (which both effectively reduce permeability) enhances the reflected shock amplitude, the transmitted wave correspondingly weakens and broadens due to stronger cumulative drag and energy dissipation, variation of the channel width has little influence on the reflected wave but leads to a decrease in transmitted-wave intensity, attributed to enhanced lateral flow separation behind the backfill.

Spatial distributions of the dimensionless pressure along the direction of shock propagation for various particle parameters is shown in Figures 7 and 8. The coordinate denotes the normalized longitudinal position, where x = 0 corresponds to the front interface of the particle cloud (backfill). Negative values represent the region of the reflected wave ahead of the backfill, while positive values correspond to the transmitted wave and the flow region behind it. The dimensionless pressure ratio is defined as p/p0, where p0 is the undisturbed gas pressure ahead of the incident shock. The plots illustrate that increasing backfill density (or decreasing permeability) intensifies the reflected shock and attenuates the transmitted wave, while larger particle diameters weaken reflection and promote a stronger transmitted front.

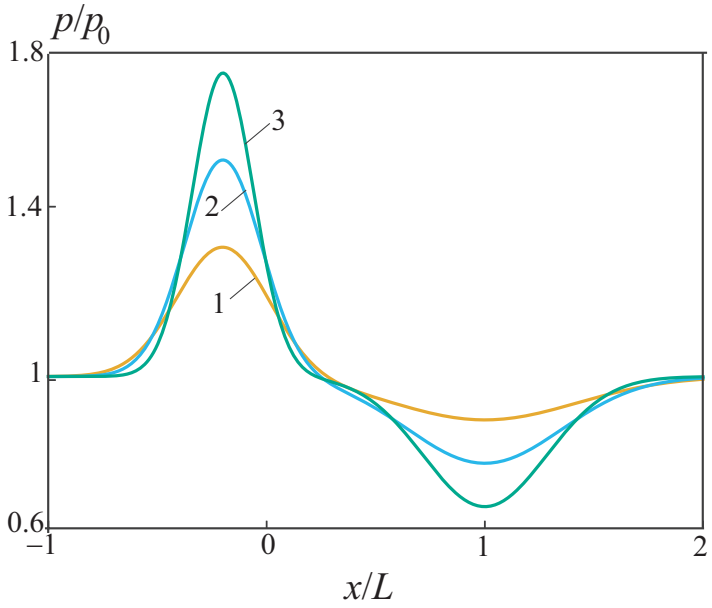


Figure 7. Distributions of the dimensionless pressure along the direction of shock propagation for various particle backfills: 10^6 (line 1), 4×10^6 (line 2), 8×10^6 (line 3).

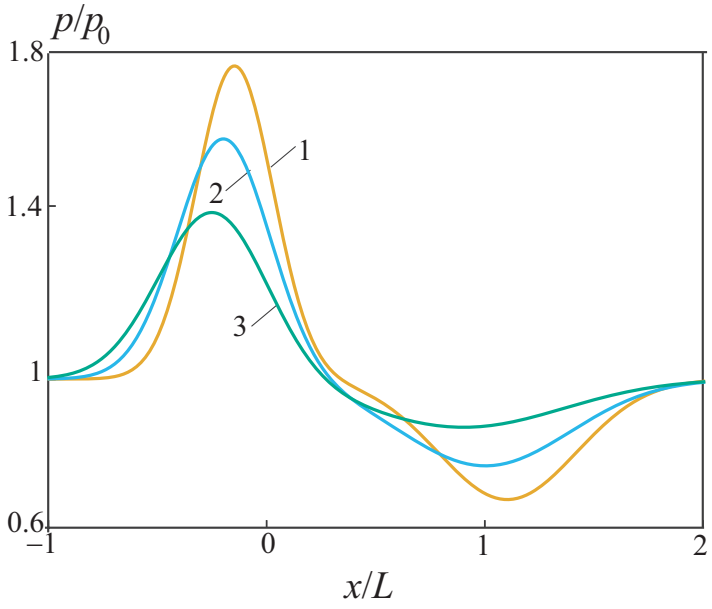


Figure 8. Distributions of the dimensionless pressure along the direction of shock propagation for various particle diameters: 50 μm (line 1), 100 μm (line 2), 200 μm (line 3).

The solid particles absorb part of the shock energy through drag and unsteady forces, leading to the formation of a weakened transmitted wave and an expanding relaxation zone downstream of the cloud. The pressure rise ahead of the cloud and the secondary compression behind it are interpreted as the result of wave reflection at the gas–particle interface and recompression due to particle inertia. This effect is consistent with the impedance mismatch between the particle-laden region and the pure gas. A higher particle loading increases the effective resistance to gas motion, resulting in a stronger reflected wave and a greater reduction in transmitted shock strength, a trend consistent with available experimental and numerical studies [23,31]. The extended pressure relaxation region observed behind the cloud is attributed to particle–gas non-equilibrium, as particles lag behind the gas phase due to finite relaxation time. This produces spatial gradients of pressure and velocity that gradually equilibrate farther downstream.

6. Conclusions

A mathematical model describing unsteady gas flows with inert particles, arising from the interaction of a shock wave with a particle cloud, is constructed within the framework of the interpenetrating continuum model. The gas and dispersed phases are represented by sets of equations expressing the conservation of mass, momentum, and energy, with interphase interactions accounted for via source terms on the right-hand sides. The governing equations for both phases are hyperbolic and can be written in conservative form, enabling the use of high-order Godunov-type methods for numerical solution. Time discretization is performed using the third-order Runge–Kutta method.

A numerical simulation is performed for the interaction of a supersonic flow with a rectangular particle cloud, initially at rest. The shock-wave structure of the flow, as well as the spatial and temporal distributions of particle concentration and other flow parameters, are analyzed. The results of the two-dimensional calculations show good agreement with those obtained from the one-dimensional model. Although the positions of the reflected and transmitted shock wave fronts are similar in both models, the one-dimensional model does not capture the fluctuations in flow parameters observed in the two-dimensional calculations.

The results enable an estimation of shock wave attenuation by a granular backfill. The calculations indicate that the intensity of the reflected wave increases with increasing backfill length, decreasing particle diameter, and decreasing backfill permeability.

Funding: This research received no external funding.

Data Availability Statement: The original contributions presented in this study are included in the article. Further inquiries can be directed to the corresponding author.

Conflicts of Interest: The author declares no conflicts of interest.

References

1. Eckhoff, R. *Dust Explosions in the Process Industries*; Gulf Professional Publishing: Houston, TX, USA, 2003; 720p.
2. Brennen, C.E. *Fundamentals of Multiphase Flows*; Cambridge University Press: Cambridge, UK, 2005; 410p.
3. Volkov, K.N.; Emelaynov, V.N. *Gas-Particle Flows*; Publishing House of Physical and Mathematical Literature: Moscow, Russia, 2008; 598p.
4. Volkov, K.N.; Derugin, Y.N.; Emelaynov, V.N.; Kozelkov, A.S.; Teterina, I.V. *Finite Difference Schemes in Gas Dynamics Problems on Unstructured Meshes*; Publishing House of Physical and Mathematical Literature: Moscow, Russia, 2015; 416p.
5. Ben-Dor, G. Dust entrainment by means of a planar shock induced vortex over loose dust layers. *Shock Waves* **1995**, *4*, 285–288. [CrossRef]
6. Lhuillier, D.; Chang, C.-H.; Theofanous, T.G. On the quest for a hyperbolic effective-field model of disperse flows. *J. Fluid Mech.* **2013**, *731*, 184–194. [CrossRef]

7. Theofanous, T.G.; Mitkin, V.; Chang, C.H. The dynamics of dense particle clouds subjected to shock waves. Part 1. Experiments and scaling laws. *J. Fluid Mech.* **2016**, *792*, 658–681. [CrossRef]
8. Theofanous, T.G.; Chang, C.-H. The dynamics of dense particle clouds subjected to shock waves. Part 2. Modeling/numerical issues and the way forward. *Int. J. Multiph. Flow* **2017**, *89*, 177–206. [CrossRef]
9. Regele, J.D.; Rabinovitch, J.; Colonius, T.; Blanquart, G. Numerical modeling and analysis of early shock wave interactions with a dense particle cloud. In Proceedings of the 42nd AIAA Fluid Dynamics Conference and Exhibit, New Orleans, LA, USA, 25–28 June 2012; AIAA 2012-3161.
10. Regele, J.D.; Rabinovitch, J.; Colonius, T.; Blanquart, G. Unsteady effects in dense, high speed, particle laden flows. *Int. J. Multiph. Flow* **2014**, *61*, 1–13. [CrossRef]
11. Wagner, J.L.; Beresh, S.J.; Kearney, S.P. A multiphase shock tube for shock wave interactions with dense particle fields. *Exp. Fluids* **2012**, *5*, 1507–1517. [CrossRef]
12. Clemins, A. Representation of two-phase flows by volume averaging. *Int. J. Multiph. Flow* **1988**, *14*, 81–90. [CrossRef]
13. Jacobs, G.B.; Don, W.S.; Dittman, T. Computation of normal shocks running into a cloud of particles using a high-order particle-source-in-cell method. In Proceedings of the 47th AIAA Aerospace Sciences Meeting including The New Horizons Forum and Aerospace Exposition, Orlando, FL, USA, 5–8 January 2009; AIAA 2009-1310.
14. Dittmann, T.B.; Jacobs, G.B.; Don, W.S. Dispersion of a cloud of particles by a moving shock: Effects of shape, angle of incidence and aspect ratio. In Proceedings of the 49th AIAA Aerospace Sciences Meeting including the New Horizons Forum and Aerospace Exposition, Orlando, FL, USA, 4–7 January 2011; AIAA 2011-441.
15. Hosseinzadeh-Nik, Z.; Subramaniam, S.; Regele, J.D. Investigation and quantification of flow unsteadiness in shock-particle cloud interaction. *Int. J. Multiph. Flow* **2018**, *101*, 186–201. [CrossRef]
16. Sen, O.; Gaul, N.J.; Davis, S.; Choi, K.K.; Jacobs, G.; Udaykumar, H.S. Role of pseudo-turbulent stresses in shocked particle clouds and construction of surrogate models for closure. *Shock Waves* **2018**, *28*, 579–597. [CrossRef]
17. Mehta, Y.; Neal, C.; Salari, K.; Jackson, T.L.; Balachandar, S.; Thakur, S. Propagation of a strong shock over a random bed of spherical particles. *J. Fluid Mech.* **2018**, *839*, 157–197. [CrossRef]
18. Theofanous, T.G.; Mitkin, V.; Chang, C.-H. Shock dispersal of dilute particle clouds. *J. Fluid Mech.* **2018**, *841*, 732–745. [CrossRef]
19. Osnes, A.N.; Vartdal, M.; Omang, M.G.; Pettersson Reif, B.A. Computational analysis of shock-induced flow through stationary particle clouds. *Int. J. Multiph. Flow* **2019**, *114*, 268–286. [CrossRef]
20. Medvedev, S.P.; Frolov, S.M.; Gelfand, B.E. Attenuation of shock waves by granular material nozzles. *J. Eng. Phys. Thermophys.* **1990**, *58*, 924–928.
21. Utkin, P.S. Mathematical modeling of the interaction of a shock wave with a dense particle bed within the framework of the two-fluid approach. *Chem. Phys.* **2017**, *36*, 61–71.
22. Abe, A.; Takayama, K.; Itoh, K. Experimental and numerical study of shock wave propagation over cylinders and spheres. *Trans. Model. Simul.* **2001**, *30*, 209–218.
23. Rogue, X.; Rodriguez, G.; Haas, J.F.; Saurel, R. Experimental and numerical investigation of the shock-induced fluidization of a particles bed. *Shock Waves* **1998**, *8*, 29–45. [CrossRef]
24. Mehrabadi, M.; Tenneti, S.; Garg, R.; Subramaniam, S. Pseudo-turbulent gas-phase velocity fluctuations in homogeneous gas-solid flow: Fixed particle assemblies and freely evolving suspensions. *J. Fluid Mech.* **2015**, *770*, 210–246. [CrossRef]
25. Sun, B.; Tenneti, S.; Subramaniam, S.; Koch, D.L. Pseudo-turbulent heat flux and average gas-phase conduction during gas-solid heat transfer: Flow past random fixed particle assemblies. *J. Fluid Mech.* **2016**, *798*, 299–349. [CrossRef]
26. Shotorban, B.; Balachandar, S. Particle concentration in homogeneous shear turbulence simulated via lagrangian and equilibrium Eulerian approaches. *Phys. Fluids* **2006**, *18*, 065105. [CrossRef]
27. Shotorban, B.; Balachandar, S. A Eulerian model for large-eddy simulation of concentration of particles with small stokes numbers. *Phys. Fluids* **2007**, *19*, 118107. [CrossRef]
28. Shotorban, B.; Balachandar, S. Two-fluid approach for direct numerical simulation of particle-laden turbulent flows at small stokes numbers. *Phys. Rev. E* **2009**, *79*, 056703.
29. Shotorban, B.; Jacobs, G.B.; Ortiz, O.; Truong, Q. An Eulerian model for particles nonisothermally carried by a compressible fluid. International. *J. Heat Mass. Transf.* **2013**, *65*, 845–854. [CrossRef]
30. Bulat, P.V.; Ilina, T.E.; Volkov, K.N.; Silnikov, M.V.; Chernyshov, M.V. Interaction of a shock wave with a cloud of particles and effect of particles on the shock wave weakening. *Acta Astronaut.* **2017**, *135*, 131–138. [CrossRef]
31. Volkov, K. Interaction of a dense layer of solid particles with a shock wave propagating in a tube. *Aerospace* **2024**, *11*, 850. [CrossRef]
32. Pandya, R.V.R.; Mashayek, F. Two-fluid large-eddy simulation approach for particle-laden turbulent flows. *Int. J. Heat Mass Transf.* **2002**, *45*, 4753–4759. [CrossRef]
33. Mashayek, F.; Pandya, R.V.R. Analytical description of particle/droplet-laden turbulent flows. *Prog. Energy Combust. Sci.* **2003**, *29*, 329–378. [CrossRef]

34. Verman, B.; Geurts, B.; Kuerten, H. Realizability conditions for the turbulent stress tensor in large-eddy simulation. *J. Fluid Mech.* **1994**, *278*, 351–362. [CrossRef]
35. Gicquel, L.; Givi, P.; Jaberi, F.; Pope, S. Velocity filtered density function for large eddy simulation of turbulent flows. *Phys. Fluids* **2002**, *14*, 1196–1213. [CrossRef]
36. Saito, T. Numerical analysis of dusty-gas flows. *J. Comput. Phys.* **2002**, *176*, 129–144. [CrossRef]
37. Laurent, F.; Massot, M.; Villedieu, P. Eulerian multi-fluid modeling for the numerical simulation of coalescence in polydisperse dense liquid sprays. *J. Comput. Phys.* **2004**, *194*, 505–543. [CrossRef]
38. Kah, D.; Laurent, F.; Massot, M.; Jay, S. A high order moment method simulating evaporation and advection of a polydisperse liquid spray. *J. Comput. Phys.* **2012**, *231*, 394–422. [CrossRef]
39. Le Veque, R.J. *Finite Volume Methods for Hyperbolic Problems*; Cambridge University Press: New York, NY, USA, 2002; 546p.
40. Godunov, S.K. Difference method of numerical calculation of discontinuous solutions of hydrodynamic equations. *Math. Collect.* **1959**, *47*, 271–306.
41. Khmel, T.A.; Fedorov, A.V. Numerical technologies for studying heterogeneous detonation of gas suspensions. *Math. Model.* **2006**, *18*, 49–63.
42. Tunik, Y.V. Global modelling of heat release during initiation and propagation of detonation and deflagration waves in methane-air-particle systems. *Shock Waves* **1999**, *9*, 173–179. [CrossRef]
43. Zhang, F.; Frost, D.L.; Thibault, P.A.; Murray, S.B. Explosive dispersal of solid particles. *Shock Waves* **2001**, *10*, 431–443. [CrossRef]
44. Benkiewicz, K.; Hayashi, A.K. Two-dimensional numerical simulations of multi-headed detonations in oxygen-aluminum mixtures using an adaptive mesh refinement. *Shock Waves* **2003**, *13*, 385–402.
45. Ludwig, T.; Roth, P. Modeling of laminar combustion wave propagation in reactive gas/particle mixtures. *Int. J. Multiph. Flow* **1997**, *23*, 93–111. [CrossRef]
46. Murray, S.B.; Zhang, F.; Thibault, P.A. Transition from deflagration to detonation in an end multiphase slug. *Combust. Flame* **1998**, *114*, 13–25.
47. Zhdan, S.A.; Prokhorov, E.S. Calculation of the cellular structure of spray detonation in the H_2–O_2 system. *Combust. Explos. Shock Waves* **2000**, *36*, 111–112.
48. Papalexandris, M.V. Numerical simulation of detonations in mixtures of gases and solid particles. *J. Fluid Mech.* **2004**, *507*, 95–142. [CrossRef]
49. Smirnov, N.N.; Nikitin, V.F.; Legros, J.C. Ignition and combustion of turbulized dust-air mixtures. *Combust. Flame* **2000**, *123*, 46–67. [CrossRef]
50. Tsuboi, N.; Hayashi, A.K.; Matsumoto, Y. Three-dimensional parallel simulation of cornstarch-oxygen two-phase detonation. *Shock Waves* **2000**, *10*, 277–285. [CrossRef]
51. Kutyshev, A.G.; Rodionov, S.P. Plane detonation waves in gas suspensions of unitary fuel with spatially non-uniform distribution of particles. *Combust. Explos. Shock Waves* **1998**, *34*, 103–110.
52. Loth, E.; Sivier, S.; Baum, J. Dusty detonation simulations with adaptive unstructured finite elements. *AIAA J.* **1997**, *35*, 1018–1024. [CrossRef]
53. Veyssiere, B.; Bozier, O.; Khasainov, B.A. Effect of a suspension of magnesium particles on the detonation characteristics of methane-oxygen-nitrogen mixtures at elevated initial pressures. *Shock Waves* **2002**, *12*, 227–233. [CrossRef]
54. Chang, E.J.; Kailasanath, K. Shock wave interactions with particles and liquid fuel droplets. *Shock Waves* **2003**, *12*, 333–341. [CrossRef]
55. Khmel, T.A.; Fedorov, A.V. Interaction of a shock wave with a cloud of aluminum particles in a channel. *Combust. Explos. Shock Waves* **2002**, *38*, 89–98. [CrossRef]
56. Fedorov, A.V.; Khmel, T.A. Numerical modeling of formation of cellular heterogeneous detonation of aluminum particles in oxygen. *Combust. Explos. Shock Waves* **2005**, *41*, 84–98. [CrossRef]
57. Gentry, R.A.; Martin, R.E.; Daly, B.J. An Eulerian differencing method for unsteady compressible flow problems. *J. Comput. Phys.* **1966**, *1*, 87–118. [CrossRef]
58. Fedorov, A.V.; Khmel, T.A. Mathematical modeling of detonation processes in a gas suspension of coal particles. *Combust. Explos. Shock Waves* **2002**, *38*, 103–112. [CrossRef]
59. Schwendeman, D.W.; Wahle, C.W.; Kapila, A.K. The Riemann problem and a high-resolution Godunov method for a model of compressible two-phase flow. *J. Comput. Phys.* **2006**, *212*, 490–526. [CrossRef]
60. Jacobs, G.B.; Don, W.S. A high-order weno-z finite difference based particle-source-in-cell method for computation of particle-laden flows with shocks. *J. Comput. Phys.* **2009**, *228*, 1365–1379. [CrossRef]
61. Sengupta, K.; Shotorban, B.; Jacobs, G.B.; Mashayek, F. Spectral-based simulations of particle-laden turbulent flows. *Int. J. Multiph. Flow* **2009**, *35*, 811–826. [CrossRef]
62. Fedorov, A.V. Structure of heterogeneous detonation of aluminum particles dispersed in oxygen. *Combust. Explos. Shock Waves* **1992**, *28*, 82–83. [CrossRef]

63. Montagne, J.L.; Yee, H.C.; Vinokur, M. Comparative study of high-resolution shock-capturing schemes for a real gas. *AIAA J.* **1989**, *27*, 1332–1346. [CrossRef]
64. Larrouturou, B. How to preserve the mass fraction positivity when computing compressible multi-component flows. *J. Comput. Phys.* **1991**, *95*, 59–84. [CrossRef]
65. Abgrall, R. How to prevent pressure oscillations in multicomponent flow calculations: A quasi conservative approach. *J. Comput. Phys.* **1996**, *125*, 150–160. [CrossRef]

Disclaimer/Publisher's Note: The statements, opinions and data contained in all publications are solely those of the individual author(s) and contributor(s) and not of MDPI and/or the editor(s). MDPI and/or the editor(s) disclaim responsibility for any injury to people or property resulting from any ideas, methods, instructions or products referred to in the content.